Title
Optical Characterization of Plasmonic Metamaterials

Author
Cho, David Jaeyun

Publication Date
2012

Peer reviewed|Thesis/dissertation

Optical Characterization of Plasmonic Metamaterials

by

David Jaeyun Cho

A dissertation submitted in partial satisfaction of the

requirements for the degree of

Doctor of Philosophy

in

Physics

and the Designated Emphasis

in

Nanoscale Science and Engineering

in the

Graduate Division

of the

University of California, Berkeley

Committee in charge:

Professor Yuen-Ron Shen, Co-Chair

Professor Feng Wang, Co-Chair

Professor Michael Crommie

Professor Xiang Zhang

Spring 2012

Optical Characterization of Plasmonic Metamaterials

David Jaeyun Cho

Abstract

Optical Characterization of Plasmonic Metamaterials

by

David Jaeyun Cho

Doctor of Philosophy in Physics

and the Designated Emphasis in Nanoscale Science and Engineering

University of California, Berkeley

Professor Yuen-Ron Shen, Co-Chair

Professor Feng Wang, Co-Chair

Optical metamaterials are artificially engineered structures composed of subwavelength units. They exhibit exotic optical properties that are unobserved or unattainable in nature. Recent efforts have led to the observation of many interesting phenomena and as well as promising applications such as super-resolution imaging and transformation optics. At optical frequencies, the functionalities of metamaterials are achieved through excitation of plasmons as most structures are metal-dielectric composites. The objective of this dissertation is to provide the tools and study the unique properties and novel phenomena of plasmonic metamaterials.

We first theoretically study a pair of nanobars to properly understand artificial magnetism which is important in most metamaterials. Then we experimentally investigate the optical properties of the "fishnet" metamaterial using a variety of spectroscopic techniques. First, we probe the plasmonic band structure using angle- and polarization- resolved linear spectroscopy. Most interestingly, we observe dark magnetic modes and their coupling to bright modes leading to avoid-crossing behavior typical of quantum systems. The k-dependent effective optical constants are measured through phase measurements confirming the dispersion of the magnetic resonance. Second, second-harmonic generation spectroscopy is carried out showing significant resonance enhancement achieved through the excitation of plasmons. The observations are substantiated with theory to validate our physical understanding of nonlinear wave-mixing processes in metamaterials. Finally, we carry out pump-probe spectroscopy to understand the dynamic behavior. The optical responses are shown to be modulated in femtosecond time scale. The modulation magnitude is greatly enhanced while the dynamics is mainly determined by the constituting dielectric medium.

Contents

Chapter 1

Introduction

1.1 Introduction

Light-matter interaction has been always of great importance in condensed matter physics. This is because materials with unique optical properties lead to novel optical phenomena of physical interest and also many useful applications. In previous years, much research has focused on *engineering* materials to control the light-matter interaction. For example, research on quantum well structures show that absorption properties can be tuned by controlling the thickness of thin semiconductor layers [1]. Studies on photonic crystals show that the diffraction of light can be precisely controlled by repeating regions of high and low dielectric constant materials [2].

More recently metal nanostructures have been in the spotlight. One reason is that metal nanostructures can have extremely strong coupling with light due to their large free electron density. This allows the scattering cross section to be several times larger than its geometrical size at the plasmon resonance [3]. A second more practical reason is that advances in nanofabrication techniques such as e-beam lithography and focused-ion beam milling have opened up the possibility of fabricating arbitrary shapes of nanostructures [4, 5]. This advancement realized the concept of metamaterials where light-matter interaction can be controlled in a highly desired way.

1.2 Optical metamaterials

Metamaterials can be defined as artificial structures composed of units with dimensions smaller than the wavelength of interest. The subwavelength feature size allows one to apply the effective medium approximation and homogenize the response [6]. As a result, the assembly of individual units can be assigned effective material properties at a macroscopic level. The individual units can be considered as artificial “atoms” or “molecules” interacting with electromagnetic waves. The effective material properties arising from the interaction is

determined by the *shape* of the subwavelength units rather than the intrinsic properties of the constituting materials. Particularly, at optical frequencies, the units are metal-dielectric composites in order to excite plasmons.

It is well known that the electric permittivity and magnetic permeability are useful optical constants that describe light-matter interaction. Maxwell equations' govern the response of the electromagnetic field in a medium. Physically, one can understand that the permittivity (ε) relates the material response to the electric field and the permeability (μ) relates the response to the magnetic field. The "material parameter space" shown in Fig. 1.1 is informative to grasp the set of all materials possible. The first quadrant (region 1) represents most common dielectric materials where ε and μ are both positive. For region 2, μ is positive but ε is negative. Metals and doped semiconductors fall in this region below their plasma frequency. Region 4 includes several ferrites but only at below microwave frequencies. Our focus is on Region 3 when both ε and μ are negative. No natural material is known to exist; thus it is very intriguing to obtain materials in this region. Particularly at optical frequencies, all conventional materials are confined to an extremely narrow line at μ=1. However, recent developments in metamaterials have allowed us to reach effective material parameters in region 3.

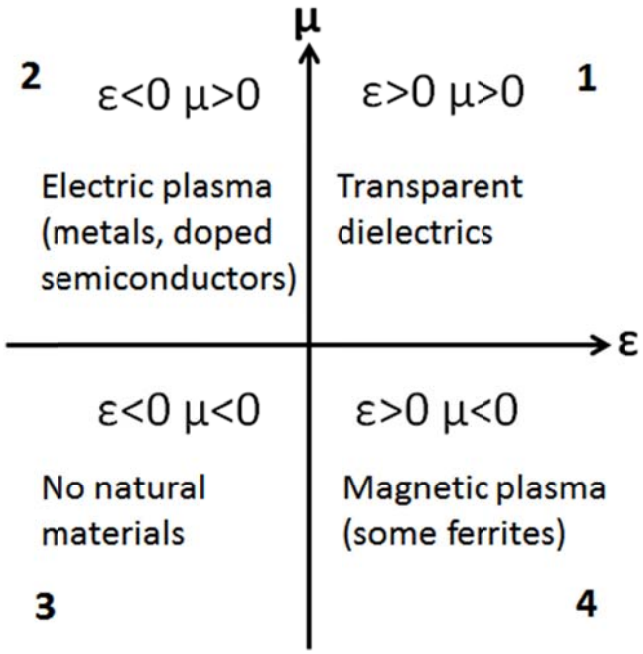

Figure 1.1 Materials parameter space

1.3 Artificial magnetism

One of the main challenges in designing artificial materials is to induce negative permeability. This is particularly difficult because the magnetic response of natural materials fades away above gigahertz frequencies [7]. There are only a few materials such as MnF_2 and EuO that have magnetic response above microwave frequencies [8, 9].

In metamaterials, artificial magnetism is obtained by carefully designing the shape of the individual units. This is achieved by creating a structure where the electromagnetic field can induce a current distribution resembling a loop. Thus, the induced current loop acts as a magnetic moment. This moment can be quite strong when the response is dramatically enhanced through a resonance. Historically, the split ring resonator (SRR) was first proposed and elucidates this key idea very well [10]. The structure composes of two concentric rings with openings as depicted in Fig. 1.2. It is shown that they can be equivalently considered as a LC circuit with a resonant frequency at $\omega_r = 1/\sqrt{LC}$ where L and C is the inductance and capacitance of the SRR. Detailed derivations [10] show that the effective permeability is given by

$$\mu_{eff} = 1 - \frac{F\omega^2}{\omega^2 - \omega_r^2 + i\Gamma\omega} \tag{1.1}$$

where the resonant frequency is

$$\omega_r = \sqrt{\frac{3dc_0^{\ 2}}{\pi^2 r^3}}\ , \tag{1.2}$$

the filling ratio F , and damping factor Γ is

$$F = \frac{\pi r^2}{a^2} \text{ and } \Gamma = \frac{2\sigma}{r\mu_0}. \tag{1.3}$$

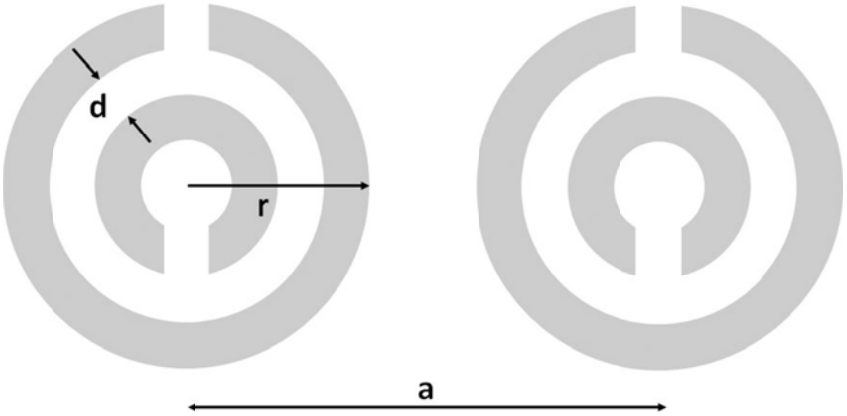

Figure 1.2 Split ring resonator with artificial magnetism

As an example, with $r = 2\times10^{-3}m$, $a = 5\times10^{-3}m$, $d = 1\times10^{-3}m$, and $\sigma = 2ohm$, the effective permeability is calculated using Eq. (1.1). As seen in Fig. 1.3, the Lorentzian resonance can be clearly identified by the real and imaginary parts of μ_{eff}. With a sufficiently

strong resonance, the effective permeability becomes negative ($\mathrm{Re}(\mu_{eff}) < 0$) in the range of $\omega_p < \omega < \omega_{mp}$. Here, ω_{mp} is defined as the effective magnetic plasma given as

$$\omega_{mp} = \frac{\omega_r}{\sqrt{1-F}} \tag{1.4}$$

at which the effective permeability becomes zero.

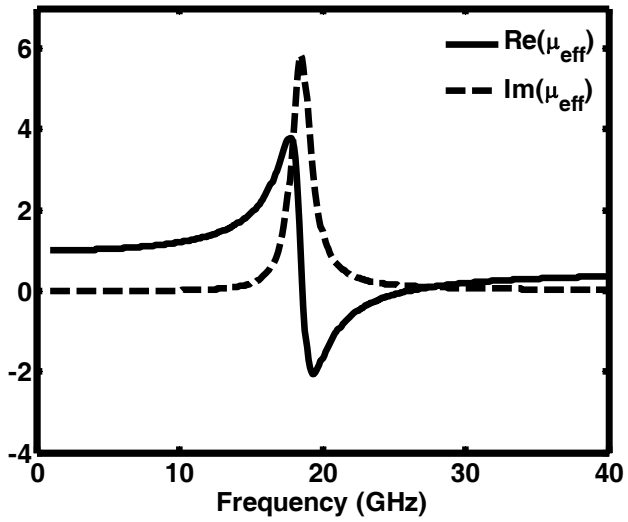

Figure 1.3 The effective permeability of a split ring resonator at microwave frequencies.

The exact resonant frequency and oscillator strength is determined by the dimensions of the SRR. This allows one to tune the range of the effective permeability to be negative. Later on, by using variant forms of the SRR, researchers have successfully pushed the resonant frequency to be at optical frequencies [11, 12]. It has now become common to use designs which are variants of a pair of bars; current loops can be obtained by exciting asymmetric modes in the pair. Detailed discussion of these properties will follow in Chapter 2.

1. 4 Negative index materials

The previous section discussed how artificial magnetism and negative effective permeability (μ_{eff}) is achieved in metamaterials. On the other hand, obtaining negative effective permittivity (ε_{eff}) is simpler because metal exhibits a strong negative permittivity below its plasma frequency. To achieve specific negative values at a certain frequency range, one only needs to design thin metal wires; they act as diluted metal with a red-shifted plasma frequency due to the reduced free electron density [13]. By overlapping thin wire arrays with negative ε_{eff}

and metamaterial units with negative μ_{eff}, one can obtain a final metamaterial structure with both negative ε_{eff} and μ_{eff}. This approach was confirmed to be successful by Smith [14].

Having simultaneous negative values of permittivity and permeability leads to quite interesting phenomena. The refractive index becomes negative and the directions of phase advance and energy flow become anti-parallel. This can be understood by considering Maxwell's equations

$$\begin{aligned} \nabla \bullet \vec{D} &= \rho, \qquad \nabla \times \vec{E} = -\frac{\partial \vec{B}}{\partial t} \\ \nabla \bullet \vec{B} &= 0, \qquad \nabla \times \vec{H} = \vec{j} + \frac{\partial \vec{D}}{\partial t} \end{aligned} \tag{1.5}$$

with the constitutive equations

$$\begin{aligned} \vec{D} &= \varepsilon \vec{E} \\ \vec{B} &= \mu \vec{H} \end{aligned} . \tag{1.6}$$

Considering a propagating monochromatic plane wave with $\vec{E}(\omega, \vec{k}) = \vec{E}_0 \exp(i\vec{k} \cdot \vec{r} - i\omega t)$ and $\vec{H}(\omega, \vec{k}) = \vec{H}_0 \exp(i\vec{k} \cdot \vec{r} - i\omega t)$, the equations can be simplified as

$$\vec{k} \times \vec{E} = \mu\omega\vec{H} \qquad \text{and} \qquad \vec{k} \times \vec{H} = -\varepsilon\omega\vec{E} . \tag{1.7}$$

It can be easily seen that $\vec{k}$, $\vec{E}$, and $\vec{H}$ form a right-handed triplet of vectors when $\varepsilon > 0$ and $\mu > 0$. On the contrary, when $\varepsilon < 0$ and $\mu < 0$, they form a left-handed triplet. In this case, the energy flow, described by the Poynting vector ($\vec{S} = \vec{E} \times \vec{H}$) is anti-parallel to the wavevector $\vec{k}$. Veselago [15] proved that in this case, the refractive index must be taken the negative sign so that causality is conserved. This is the reason why negative-index materials are also called as left-handed materials.

Negative-index materials exhibit many counter-intuitive phenomena as discussed in Veselago's paper [15]. The study was limited theoretically as there was no material available exhibiting simultaneous negative values. One interesting result is that when light is incident from a positive-index material to a negative-index material, the light is refracted to the negative angle direction with respect to the interface normal. Snell's law,

$$n_1 \sin\theta_1 = n_2 \sin\theta_2 \tag{1.8}$$

indeed shows that the angle of refraction is negative; if n_1 and n_2 have opposite signs, then θ_1 and θ_2 also have opposite signs. Furthermore, it was also predicted that the Doppler effect and Cherenkov effect are reversed in a negative-index medium [16].

Experimentally, negative-index medium was demonstrated at microwave frequencies using a combination of metallic wires and SRRs [14]. Continued interest and advance in

nanofabrication techniques have allowed researchers to develop negative-index materials at optical frequencies using a variety of structures such as paired nanorods, fishnet, and silver nanowires [17-19].

1.5 Thesis highlights

The potential implications of metamaterials are not just limited to having a negative refractive index. The true potential lies in the freedom to obtain desired values of the effective permittivity and permeability. Moreover, it is possible to control these values in frequency-domain as well as in the spatial-domain. This enables fascinating applications such as sub-diffraction limited imaging [20-25] and transformation optics [26-32]. Thus, the aim of this dissertation is to provide tools for characterization and fundamental understanding to facilitate the study of future metamaterials for these exciting applications.

The dissertation is organized as the following.

In Chapter 2, we theoretically study the artificial magnetism in a pair of nanobars. The various multipole components contributing to the magnetic resonance is discussed. We point out that the electric quadrupole has been incorrectly neglected in previous studies. The findings may serve as a ground work to understand the interaction between individual units.

In Chapter 3, we study the plasmonic band structure of a fishnet metamaterial. The structure is designed by electromagnetic simulation and fabricated through nanoimprint lithography. The experiment is carried out using an angle- and polarization-resolved spectroscopy technique. Our measurements allow us to identify multiple magnetic bands and understand their coupling behavior in the fishnet structure. In addition, phase measurements are carried out to deduce the k-dependent effective optical constants.

Chapter 4 describes our second-harmonic generation (SHG) spectroscopy study in optical metamaterials over the magnetic resonance. The result shows a strong enhancement of the nonlinear signal due to excitation of a plasmon resonance. Furthermore, we carried out theoretical calculations and successfully reproduce the results quantitatively confirming our physical understanding of nonlinear wave-mixing processes in metamaterial structures.

Finally, in Chapter 5, we study the dynamic response of a metamaterial through pump-probe spectroscopy. We find that optical pumping can induce drastic changes of the linear properties in femtosecond time scale. The modulation dynamics is mainly determined by the constituting dielectric medium, but the modulation magnitude is greatly enhanced through the plasmon resonance.

Chapter 2

Contribution of the electric quadrupole in artificial magnetism

2.1 Motivation

A major focus in research is designing metamaterials with negative refractive index. It was first demonstrated in microwave range [10, 33-37] and later extended to infrared and optical frequencies [11, 12, 17, 38-46]. As described in Sec. 1.4, having the effective permittivity (ε) and permeability (μ) to be simultaneously negative leads to a negative index [10, 15, 47]. It is straightforward to obtain a negative ε, which occurs naturally for metals at optical frequencies. However, negative μ is nonexistent in nature. Only recently, it was achieved in artificial metamaterials using strong magnetic resonances in suitably designed metal plasmonic nanostructures [11, 12, 19, 38, 43-45, 48]. It is usually considered as to be associated with a magnetic dipole resonance and the contribution from electric quadrupole is neglected. However, similar to the magnetic dipole radiation, the electric quadrupole radiation can also be greatly enhanced by plasmon resonances and it is typically of comparable strength at optical frequencies. Therefore, one might expect electric quadrupole to play as important a role as magnetic dipole. In most previous studies, electric quadrupole contributions to the plasmon resonance are not carefully investigated [42, 43]. Here, we show by simulation that the electric quadrupole contribution is actually comparable to that from magnetic dipole and therefore may not be ignored.

2.2 Approach

2.2.1 Parallel nanobar structure

Several metamaterial designs have been proposed for achieving negative refraction in the optical range. However, many are variants of the parallel metallic nanobar structure (Fig. 2.1) [19, 40, 42-45]. Therefore, we focus on this structure. The incident electric field polarized

along the bar can resonantly induce symmetric (Fig. 2.1(b)) or asymmetric (Fig. 2.1(c)) electron oscillations depending on the driving frequency. As illustrated in the figure, the symmetric mode is characterized by a net electric dipole ($\vec{P}$), while the asymmetric mode, arising from a current distribution with the currents in the two metal bars out of phase, is a mode of mixed magnetic-dipole and electric-quadrupole character. Generally, however, a structure may have separate resonance modes with, respectively, dominating magnetic-dipole and electric-quadrupole character.

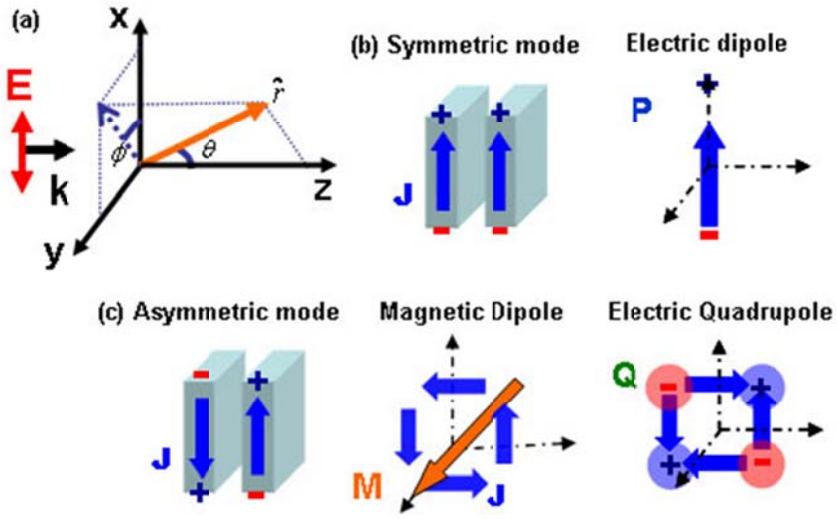

Figure 2.1 Coordinates and plasmon resonances of a pair of bars: (a) Relative coordinates of incident light with respect to the pair of bars. The incident light is propagating on the z-axis and linearly polarized along the x-axis being parallel to the long axes of the bars. (b) Symmetric electron oscillation is characterized as a net electric dipole (P). (c) Asymmetric electron oscillation is characterized as a sum of magnetic dipole (M) and electric quadrupole (Q). The arrows refer to currents and the "+" and "- signs to the charge distribution.

2.2.2 Numerical calculation

We numerically calculate the scattering intensity spectrum and the internal electric field of a single unit of parallel bar structure using the Discrete Dipole Approximation (DDA) method [49, 50]. In this method, interaction of the incoming light with the structure is described by an assembly of point dipoles distributed throughout the volume of the structure. The dipoles are induced by the local field, which is the sum of the incident field and the field created by the induced dipoles themselves. This generates a set of linearly coupled equations which are solved self-consistently. Solution of the equations yields both the local electric field distribution and far field scattering intensity in different directions. We consider two silver bars in air with cross section of 135nm × 80nm and thickness of 30nm and the bars are separated by a 25nm thick SiO_2 layer. The optical constants of silver were taken from Ref. [51].

2.3 Results and analysis

2.3.1 Far-field radiation pattern of multipoles

Fig. 2.2 shows the light scattering spectra along several directions in the x-z plane ($\phi = 0$). The beam geometry is illustrated in Fig. 2.1. The spectra exhibit two resonances at 580nm and 685nm, corresponding to symmetric and asymmetric modes, respectively. The calculated local field distribution inside the metal structure allows us to obtain the current density distribution and the multipole components of $\vec{\mathrm{P}}$, $\vec{\mathrm{M}}$, $\ddot{\mathrm{Q}}$, etc., on the structure. We can then calculate separately the complex far fields, $\tilde{E}_P$, $\tilde{E}_M$ and $\tilde{E}_Q$, generated by $\vec{\mathrm{P}}$, $\vec{\mathrm{M}}$ and $\ddot{\mathrm{Q}}$, and compare their relative strengths [52]. For the 580 nm resonance, we found that the currents in the two bars are in phase and the electric dipole radiation $\tilde{E}_P$ dominates. For the 685nm resonance, the currents are largely out of phase as expected from an asymmetric mode. The corresponding field ratio in the forward direction ($\theta = 0^\circ$) is $\left|\tilde{E}_{P_0}\right| : \left|\tilde{E}_{M_0}\right| : \left|\tilde{E}_{Q_0}\right|$ = 1: 0.81: 0.62. As the wavelength moves away from 685nm, $\left|\tilde{E}_{M_0}\right|$ and $\left|\tilde{E}_{Q_0}\right|$ decrease rapidly while $\left|\tilde{E}_{P_0}\right|$ changes only slightly. Therefore we attribute the electrical dipole field $\tilde{E}_{P_0}$ to the nonresonant contribution from the tail of the 580 nm resonance. The relative magnitude of $\tilde{E}_{M_0}$ and $\tilde{E}_{Q_0}$ shows that the contribution of the electric quadrupole is comparable to that of the magnetic dipole.

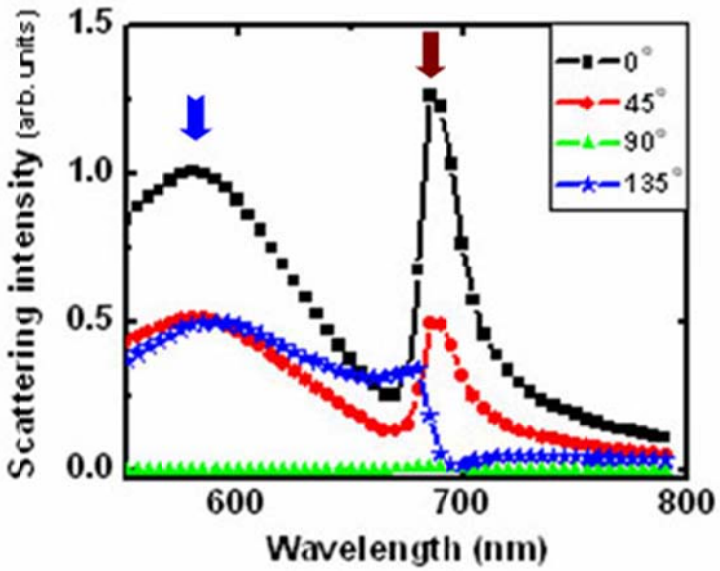

Figure 2.2 Scattering intensity spectra in the x-z plane ($\phi = 0^\circ$) for $\theta = 0°, 45°, 90°, 135°$ of a pair of parallel silver bars. θ is the angle between the incident light and the scattered light propagation directions as in Fig. 2.1. Arrow at 580nm denotes the symmetric mode resonance; arrow at 685nn denotes the asymmetric mode resonance.

We also find that other multipoles also have negligible contribution to the far field radiation. This can be seen by comparing the coherent sum of radiation from $\vec{P}$, $\vec{M}$ and $\vec{\vec{Q}}$ with that directly obtained from the DDA simulation which inherently includes radiation from all orders of multipoles. Fig. 2.3 shows the comparison for scattered radiation at 580 and 685nm in the x-z plane versus angle θ. The curves are sums of radiation calculated from $\vec{P}$, $\vec{M}$ and $\vec{\vec{Q}}$ and the dots are directly from the DDA simulation. The agreement is almost perfect. Apparently, higher order multipoles have much weaker radiation strengths that are negligible for these nanoscale structures. It is then possible to deduce $\vec{P}$, $\vec{M}$ and $\vec{\vec{Q}}$ unambiguously from the polarization-dependent and angle-resolved scattering spectra.

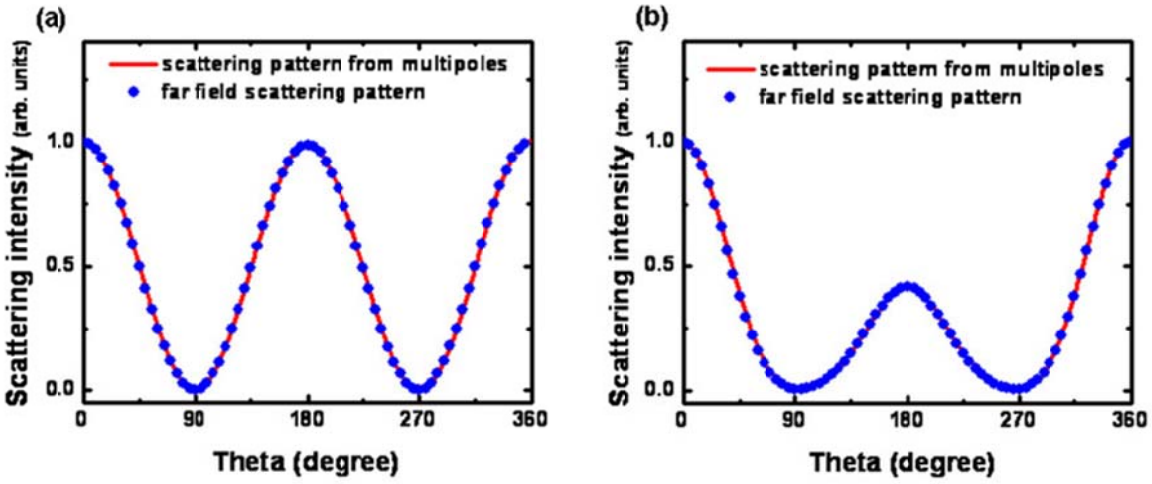

Figure 2.3 Comparison of the far field scattering pattern in the x-z plane calculated from multipoles ($\vec{P}$, $\vec{M}$, and $\vec{\vec{Q}}$) and directly from DDA calculation: (a) symmetric mode at 580nm, (b) asymmetric mode at 685nm. The solid curve corresponds to the scattering intensity calculated from $\vec{P}$, $\vec{M}$ and $\vec{\vec{Q}}$. Dots are the scattering intensity calculated directly from the DDA simulation. θ is the angle between the incident light and the scattered light propagation directions. The excellent agreement between curves and dots shows that the radiation from the parallel bar structure is dominated by $\vec{P}$, $\vec{M}$, and $\vec{\vec{Q}}$.

In experiment, for nanostructures with certain symmetry, the multipole components can be easily determined by measuring the far field radiation pattern along specific planes. For example, for the parallel bar structure in Fig. 2.1, the far fields generated from $\vec{P}$, $\vec{M}$, and $\vec{\vec{Q}}$ and propagating along $\hat{r}$ in the x-z plane are $\vec{E}_{P_0}\cos\theta$, $\vec{E}_{M_0}$, and $\vec{E}_{Q_0}\cos 2\theta$, respectively, with $\vec{E}_{P_0}$, $\vec{E}_{M_0}$, and $\vec{E}_{Q_0}$ being complex. The total scattered electric field is

$\vec{E}_{total} = (\left|\vec{E}_{P_0}\right|\cos\theta + \left|\vec{E}_{M_0}\right|e^{i\phi_M} + \left|\vec{E}_{Q_0}\right|e^{i\phi_Q}\cos 2\theta)\hat{\theta}$, where the phases ϕ_M and ϕ_Q are relative to $\vec{E}_{P_0}$. The measured scattering spectra with their polarization dependence can be fitted by the total intensity $\left|\vec{E}_{total}\right|^2 = \left|\left|\vec{E}_{P_0}\right|\cos\theta + \left|\vec{E}_{M_0}\right|e^{i\phi_M} + \left|\vec{E}_{Q_0}\right|e^{i\phi_Q}\cos 2\theta\right|^2$ to obtain $\vec{E}_{P_0}$, $\vec{E}_{M_0}$, and $\vec{E}_{Q_0}$ and hence $\vec{\mathrm{P}}$, $\vec{\mathrm{M}}$, and $\vec{\mathrm{Q}}$. To demonstrate this, we fit the far field scattering pattern directly obtained from DDA method to retrieve $\left|\tilde{E}_{P_0}\right| : \left|\tilde{E}_{M_0}\right| : \left|\tilde{E}_{Q_0}\right|$ = 1: 0.88: 0.67 whereas explicit calculation of $\vec{\mathrm{P}}$, $\vec{\mathrm{M}}$, and $\vec{\mathrm{Q}}$ gives $\left|\tilde{E}_{P_0}\right| : \left|\tilde{E}_{M_0}\right| : \left|\tilde{E}_{Q_0}\right|$ = 1: 0.81: 0.62. The agreement shows that indeed it is possible to deduce separately the multipole contributions in a scattering experiment.

2.3.2 Relation of multipoles to optical constants

We examine the contribution of $\vec{\mathrm{Q}}$ to the effective ε and μ of a metamaterial. For the parallel bar structure, $\tilde{E}_M$ and $\tilde{E}_Q$ have the same phase in the forward and backward direction at the asymmetric resonance, and may appear indistinguishable for light propagation in the corresponding metamaterial. Therefore, one may anticipate that electrical quadrupole $\vec{\mathrm{Q}}$ plays a similar role as magnetic dipole $\vec{\mathrm{M}}$ and both contribute to the effective μ.

In the case of metamaterials, one often uses $\vec{k}$-independent effective ε and μ to describe electric dipole and magnetic dipole contributions of the responses, respectively. Therefore, we investigate the description with $\vec{k}$-independent effective ε and μ with non-negligible electric quadrupole term so that simple Fresnel coefficients for transmission and reflection are still valid. To be more rigorous, we examine the effective ε and μ of a metamaterial with reference to the Maxwell equations.

We consider the simple case of an isotropic bulk metamaterial. In this case, the electric quadrupole tensor is described by $Q_{ij} = i\alpha_Q(k_i E_j + k_j E_i)$ where α_Q is a constant and k_i and E_j are the components of wavevector $\vec{k}$ and incoming electric field $\vec{E}$. The macroscopic Maxwell equations are typically written in the form,

$$\begin{aligned} &\nabla\cdot\vec{D} = 0, && \nabla\cdot\vec{B} = 0 \\ &\nabla\times\vec{E} = -\frac{1}{c}\frac{\partial\vec{B}}{\partial t}, && \nabla\times\vec{H} = \frac{1}{c}\frac{\partial\vec{D}}{\partial t} \end{aligned} \tag{2.1}$$

where

$$\vec{D} = \vec{E} + 4\pi(\vec{P} - \nabla\cdot\vec{Q}) \equiv \varepsilon(k)\vec{E}, \qquad \vec{H} = \vec{B} - 4\pi\vec{M} \equiv \mu\vec{B} \tag{2.2}$$

are the electric displacement and magnetic field, respectively. However, as we mentioned above, $\vec{D}$ and $\vec{H}$ are not uniquely defined [7, 53-55]. The macroscopic Maxwell equations are

invariant if we replace $\vec{D}$ and $\vec{H}$ in Eq. (2.2) by $\vec{D}' = \vec{E} + 4\pi\vec{P}$ and $\vec{H}' = \vec{B} - 4\pi(\vec{M} + \vec{M}_Q)$ with $\nabla \times \vec{M}_Q = -\frac{1}{c}\frac{\partial}{\partial t}\nabla \cdot \vec{Q}$. For an isotropic material, we find $\vec{M}_Q = (\frac{\omega}{c})^2 \alpha_Q \vec{B}$. Together with the materials response relations of $\vec{P} = \chi_E \vec{E}$, $\vec{M} = \chi_M \vec{B}$, it yields

$$\varepsilon = 1 + 4\pi\chi_E \ , \qquad \mu^{-1} = (1 - 4\pi\chi_M) - 4\pi(\frac{\omega}{c})^2 \alpha_Q \, , \tag{2.3}$$

where both ε and μ are $\vec{k}$ -independent and the latter contains electric quadrupole contribution. This electric quadrupole contribution can be viewed as a resonance enhanced spatial dispersion in the metamaterial. We show in [56] that the same conclusion can be reached by considering inclusion of electric quadrupole contribution in the derivation of transmission and reflection coefficients and matching them with the known Fresnel coefficients in terms of ε and μ. In this derivation, boundary conditions have to be treated with great care [53].

Although our description is shown to be valid for an isotropic material, it also holds true for light propagation in high symmetry directions in non-isotropic materials, which is often the experimental case. For instance, it applies to normal incidence of light in a fishnet metamaterial, where negative refractive index has been reported.

2.4 Conclusions

In summary, we have shown that metamaterials consisting of a pair of metal bars or similar nanostructures may have electric quadrupole resonances comparable to magnetic dipole resonances in strength at the resonant frequency. Light scattering spectroscopy on a unit nanostructure should allow separate determination of the different multipole components at various resonant frequencies and hence the nature of the resonances. In an isotropic metamaterial or anisotropic metamaterial with wave propagating along high symmetry directions, the nonnegligible electric quadrupole appears to contribute to the effective μ. This implies that electric quadrupole contribution may also yield a negative μ near its resonance in a metamaterial. Generally, electric quadrupole resonance can appear at a different frequency from the magnetic dipole resonance and may alone give rise to negative μ. It is incorrect to neglect the electric quadrupole in describing artificial magnetism in optical metamaterials.

Chapter 3

Probing the plasmonic band structure of optical metamaterials

3.1 Motivation

At optical frequencies, metamaterials achieve their functionality by excitation of plasmon resonances [19]. The individual units can be considered as *meta-atoms*. Since the units are typically arranged in a lattice, a plasmonic band structure appears in analogy to the electronic band structure of solids. Here, the excited plasmon modes take the role of the electronic orbitals. The shape of the Brillouin Zone (BZ) will be defined by the lattice arrangement of the meta-atoms. Understanding the plasmonic band structure of a given metamaterial is important because applications such as sub-diffraction imaging [20-22, 24] and cloaking [26-32] require precise control of the optical responses depending on the wave propagation direction, i.e., the wavevector in the BZ. In this respect, theoretical and experimental studies have investigated the oblique response of metamaterials with much attention to the magnetic split ring resonator (SRR) [57-60]. It has been shown that they can exhibit non-dispersive responses at terahertz or lower frequencies and thus could be used for imaging and cloaking applications. At optical frequencies, similar attempts have been carried out [61-63] to report that the optical responses exhibit strong angle-dependence and therefore the dispersion cannot be ignored. However, the studies are limited as only high symmetry directions of the dispersion are probed and do not consider all the involved plasmon modes. Therefore, here we study the plasmon band structure of a metamaterial in several directions of its BZ to fully characterize its plasmon resonances. By doing so, we are able to identify previously unobserved magnetic resonances and also interesting coupling behavior between adjacent modes. The approach we provide can be generally applied to investigate metamaterial structures.

In this chapter, we focus on the "fishnet" structure due to its importance in achieving negative refractive index at optical frequencies [17, 64]. Most works have focused on studying

the well known magnetic resonance only at normal incidence. More recently, it was reported that the previously overlooked higher energy resonance is also magnetic [65, 66]. But the understanding is lacking because only the normal incidence is probed and no clear physical description is provided except that the currents are antiparallel for the top and bottom metal layer. Ref. [67] measured the angle-dependent transmission spectra of the fishnet but the characterization is incomplete as only the lower energy magnetic resonance is discussed due to their limited spectra range. However, as we will show, the fishnet exhibits other magnetic modes that previous studies were unable to probe. The plasmon band structure of the fishnet requires better understanding through a systematic characterization by probing several directions of the BZ with extended spectral range.

Here, we utilize an angle- and polarization- resolved spectroscopy technique to identify the excited plasmon resonances from the spectral features of transmission, reflection, and absorption. This allowed us to observe the excitation of various plasmon resonances and their evolution with the in-plane wavevector and light polarization. In addition, we carry out phase measurements using an interferometry scheme to obtain the transmission and reflection coefficients and retrieve the k-dependent effective optical constants. From our results, we identify multiple magnetic bands and show that optically dark modes can couple to the bright bands resulting in unusual dispersion behavior. The deduced effective optical constants confirm that the plasmon dispersion is originating from the shift of the magnetic resonance.

3.2 Fishnet design and preparation

The studied fishnet structure is depicted in Fig. 3.1 with a schematic of its three dimensional structure (Fig. 3.1(a)) and a scanning electron microscope image (Fig. 3.1(b)). It is composed of top and bottom metal layers separated by a dielectric layer [64]. We choose the multilayers to be Ag/SiO_2/Ag with 28/35/28nm thickness. The structure is a square lattice with a periodicity of $a = 600\,\text{nm}$. Therefore, the BZ in reciprocal space is also a square. Our structure is fabricated by the nanoimprint lithography (NIL) technique [68]. It involves two major steps. First step is to prepare the NIL mold by patterning the fishnet on a Si substrate using electron-beam lithography. Second step is to fabricate the actual sample using this mold as a template. A double-layer UV-curable NIL process is utilized and followed by an e-beam evaporation and lift-off process. The final result is the multilayer structure as presented in Fig. 3.1. Detailed description of the fabrication process is elaborated in Ref. [69].

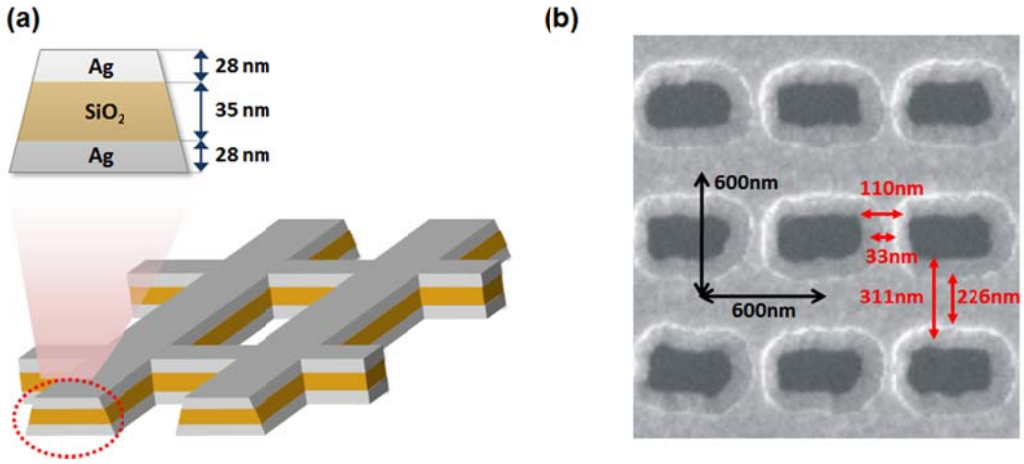

Figure 3.1 Fishnet structure (a) 3-dimensional schematic of the fishnet showing the metal-dielectric-metal multilayers of Ag(28nm)/ SiO_2 (35nm)/ Ag(28nm). (b) Scanning electron microscope image. The thin and thick wires compose of a square lattice with a periodicity of 600nm.

3.3 Plasmonic band structure of fishnet

3.3.1 Experimental scheme

To characterize the fishnet structure, we used a broadband super-continuum fiber laser providing a spectral range of 0.5-1.6μm with 5ps pulses at 20MHz repetition rate. Fig. 3.2(a) shows the experimental scheme we developed to measure the transmitted and reflected light from the sample. A half-ball lens is employed which enables us to probe the sample with an in-plane wavevector (k_t) given by

$$k_t = n_g k_0 \sin(\theta_{in}) \tag{3.1}$$

where n_g is the refractive index of the half-ball lens, k_0 is the wavevector in free space, and θ_{in} is the incident angle. The half-ball lens is rotated to choose θ_{in}. The incident light is chosen to be either s- or p-polarized.

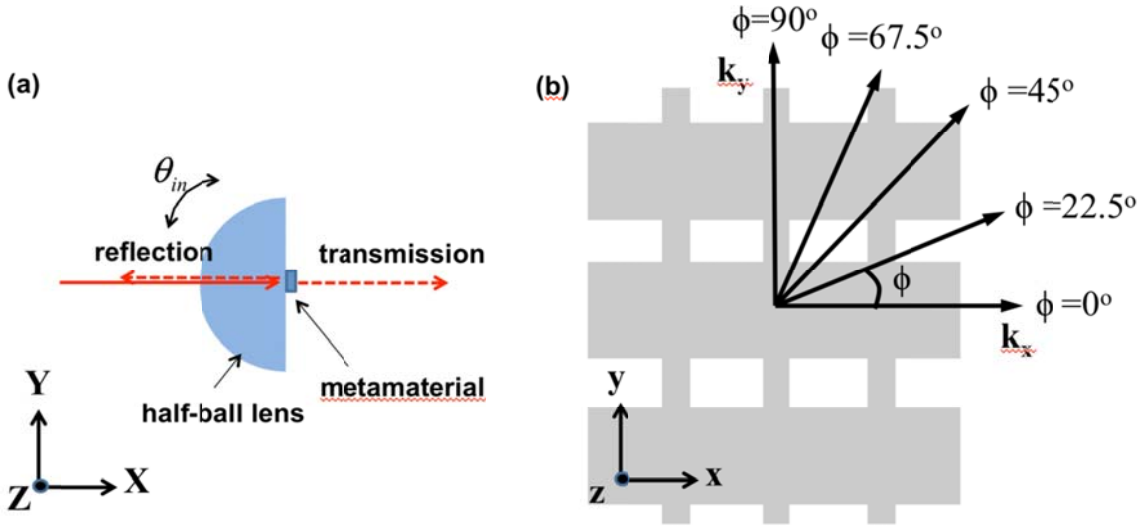

Figure 3.2 (a) Experimental scheme employing a half-ball lens on rotational stage. (b) Five directions ($\phi = 0^\circ,\ 22.5^\circ,\ 45^\circ,\ 67.5^\circ,$ and 90°) of the in-plane wavevector ($\vec{k}_t$) that are probed.

In the measurement, the sample is rotated in the XY plane of the experimental setup (Fig. 3.2(a)). We first choose the sample orientation angle (ϕ) (Fig. 3.2(b)) and align it to be parallel to the XY plane. This fixes the direction we probe in the BZ. The rotation angle determines θ_{in} and the magnitude of k_t according to Eq. (3.1). For a given set of ϕ and θ_{in}, we obtain the transmission (T) and reflection (R) spectra and deduce the absorption (A) spectra. The resonant modes can be identified from the spectral features of the obtained spectra. The resonant frequencies are deduced from the dip minima of T and peak maxima of R and A which are correlated in frequency with each other. For example, the sets of dips of T and peaks of R and A in Fig. 3.3(a) indicate the excited modes. Fig. 3.2(b) shows the five directions, i.e., $\phi = 0^\circ,\ 22.5^\circ, 45^\circ, 67.5^\circ,$ and 90°, that we chose to probe the BZ of the fishnet.

3.3.2 Results and discussion

3.3.2a Experimental results

The experimental linear spectra are presented in Fig. 3.3. Incident light is s-polarized for $\phi = 0^\circ,\ 22.5^\circ,\ 45^\circ$, and p-polarized for $\phi = 67.5^\circ,\ 90^\circ$ so that the incident electric field has a component perpendicular to the thick wires. In this section, we only report the observed modes and defer detailed discussions to later sections. In Fig. 3.3, we mark each of the identified modes as $\mathrm{R}^{\phi}_{\#}$ with a dash line where ϕ indicates the direction and $\#$ is the assigned mode name. For simplicity, we only mark the modes on the T spectra as the dips of T and peaks of R and A are correlated. First, for $\phi = 0^\circ$, as shown in Fig. 3.3(a), we observe two modes R^{0}_{1} and

R_2^0 with energies changing from 0.85eV to 0.88eV and 1.14eV to 1.02eV, respectively. We observe the mode strength of R_1^0 to decrease as its absorption reduces from 60% to 55% and that of R_2^0 to increase as its absorption grows from 30% to 45%. Second, for $\phi = 90^\circ$, we observe modes R_1^{90}, R_2^{90}, R_3^{90}, and R_{Ag/SiO_2}^{90} as marked in Fig. 3.3(b). Both R_1^{90} and R_2^{90}, which appears at 0.85eV and 1.14eV, respectively, vanishes with increasing k_t. On the other hand, R_3^{90} and R_{Ag/SiO_2}^{90} are unobservable for $k_t = 0$ but appears at finite k-vector. Finally, for $\phi = 22.5^\circ$, 45°, and 67.5°, the spectra commonly exhibit R_{1A}^{ϕ} and R_{1B}^{ϕ} (ϕ indicating the respective direction) to show avoid-crossing behavior with increasing k_t; R_{1A}^{ϕ} starting at 0.85eV initially shifts to higher energy but then shifts to lower energy when R_{1B}^{ϕ} starts to appear at 0.92eV. The dashed lines of R_{1A}^{ϕ} in Fig. 3.3(c,d,e) show this change of shift direction with increasing k_t. R_2^{ϕ}, $R_3^{67.5}$, and $R_{Ag/SiO_2}^{67.5}$ also appear in these directions and will be discussed later in detail as their modes are associated with those of R_2^{90}, R_3^{90}, and R_{Ag/SiO_2}^{90} which are examined in later sections. To summarize, we observe the modes labeled as R_1^{ϕ}, R_{1A}^{ϕ}, R_{1B}^{ϕ}, R_2^{ϕ}, R_3^{ϕ}, and R_{Ag/SiO_2}^{ϕ} depending on ϕ. The results clearly indicate that consideration of only two modes discussed in previous works is insufficient to properly describe the plasmon band structure of the fishnet. Particularly, several of the modes only appear at finite k_t. In the following section, we present a physical picture of the general modes of the fishnet before analyzing the experimental results in detail. Later in the discussion section, we will relate the observed modes to the general modes of the fishnet.

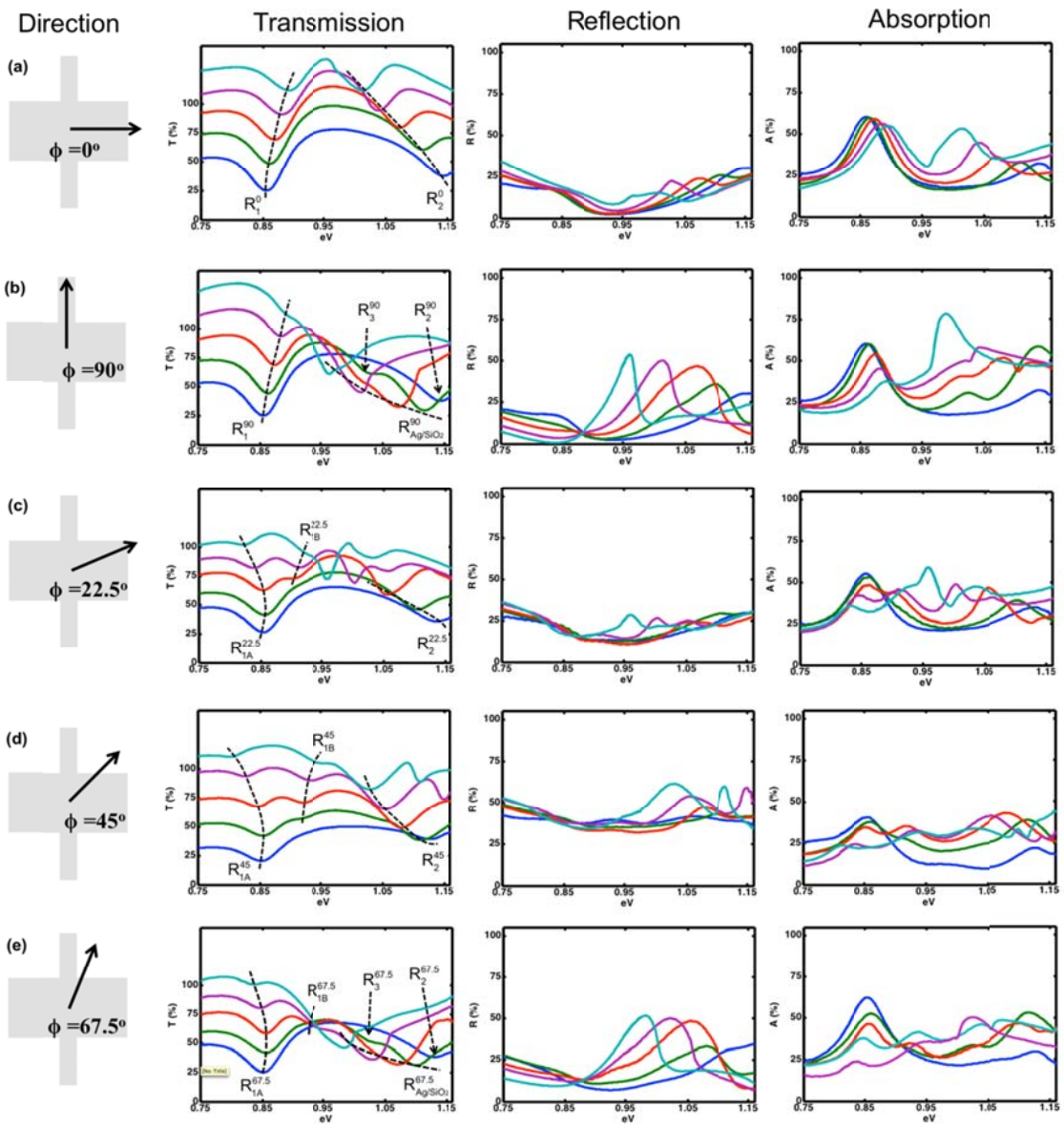

Figure 3.2 Experimentally measured transmission, reflection, and absorption spectra for (a) $\phi = 0^\circ$ (b) $\phi = 90^\circ$ (c) $\phi = 22.5^\circ$ (d) $\phi = 45^\circ$ (e) $\phi = 67.5^\circ$. The incident angles of 0°, 10°, 17°, 23°, and 29° are displayed. For clarity, the transmission spectra are vertically offset with increasing angle.

3.3.2b General picture of the plasmon modes in fishnet

The fishnet structure is essentially a metal/dielectric/metal layer with perforated holes surround by air (superstrate) and SiO_2 (substrate) on each side. It has been studied that the dispersion of the surface plasmons of a thin metallic film with holes can be well described by that without holes [70-73]. Therefore, to help our understanding of the surface plasmon modes

of the fishnet, we first consider the resonant modes of $Ag/SiO_2/Ag$ layers with the same thickness of our fishnet (Fig. 3.1(a)) but without the presence of holes. (We will refer this as the "infinite film system".) Following the method in Ref. [74], we find that three distinct modes exist in our spectral range (Fig. 3.4). (A fourth mode exists at higher energy near the plasma frequency of silver and thus is neglected in our discussion [75].) Fig. 3.4(a) shows the tangential electric field distribution of the three modes at 1eV corresponding to $k = 5.1,\ 7.4,\ \text{and}\ 12.0\mu m^{-1}$ for each mode, respectively (orange dotted line in Fig. 3.4(b)). As one can see, mode $M_{Ag/air}$ and M_{Ag/SiO_2} have its field confined more in the Ag/Air (superstrate) interface and Ag/SiO_2 (substrate) interface, respectively. The mode M_{mag} has its field confined mainly in the two Ag/SiO_2 interfaces between the metal layers. The field distribution is asymmetric and thus can be understood as magnetic modes. The dispersion of each mode is presented in Fig. 3.4(b). We note that M_{mag} has the lowest dispersion curve. Similarly, we expect that the fishnet exhibits these three distinct modes but the periodicity of their dispersion curves have to be taken into account due to the presence of the holes. (For later reference, we mark the sections I, II, and III in Fig. 3.4(b) to indicate the probed photon energy range and corresponding k-vector range for each mode.)

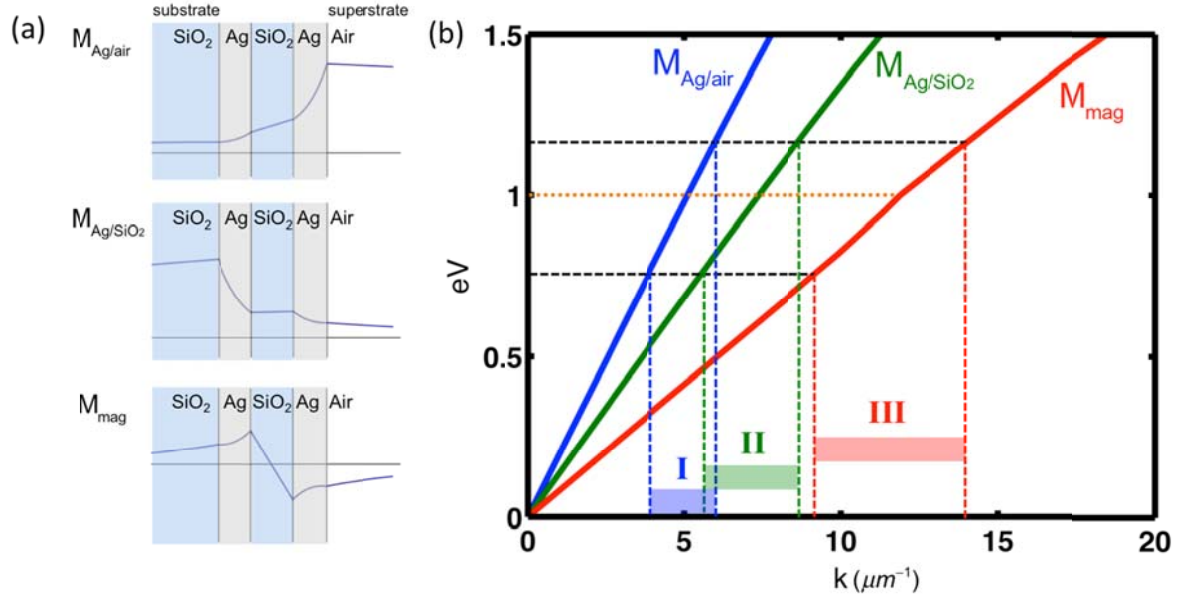

Figure 3.4 Three resonant modes of SiO_2 (substrate)/Ag (28nm)/SiO_2 (35nm)/Ag (28nm)/Air (superstrate) infinite film system lying in the near-infrared spectral range. (a) Tangential electric field distribution of three modes at 1eV (b) Dispersion curve of the three modes. Section I, II, and III are drawn to indicate the k-vector range of the corresponding probed photon energies (0.75eV~1.16eV) for each mode, respectively.

Using the mode dispersion in the infinite film system as a starting point, we can understand the plasmonic band structure of the fishnet by introducing two important effects: (1) Finite Brillouin Zone due to the periodic structure, and the corresponding formation of many

bands in the folded Brillouin zone. (2) Different boundary condition (due to the edges of the metal structure) will modify the plasmonic wavefunction and shift the plasmon resonance frequency.

Let's examine first the Brillouin Zone effect and assume the $\omega - k$ dispersion from infinite film system is little modified. The unit cell of the fishnet is a 600 nm x 600 nm square. In Fig. 3.5, we illustrate the corresponding reciprocal lattice in the extend zone scheme. The first Brillouin Zone is the region noted by the gray shade. Each red dot in the figure corresponds to a reciprocal lattice point, which will be at the Γ-point in the folded zone scheme. The blue circle encloses each reciprocal lattice point and represents the k-vector range that we can probe in the experiment. The yellow area indicates the dispersion section of the photon energy we probe for the three modes M_{Ag/SiO_2}, $M_{Ag/air}$, and M_{mag}. (Thus, the yellow area in Fig. 3.5(a,b,c) corresponds to section I, II, and III in Fig. 3.4(b), respectively.) The overlap between the blue and yellow area will then be resonances which lie in the momentum and energy range that we can probe. For resonances derived from $M_{Ag/air}$, there is no overlap between the blue and yellow area (Fig. 3.5(a)) indicating that the mode is outside the probing range. Second, for M_{Ag/SiO_2}, there are overlapping regions in the second Brillouin zone, indicating a single branch of resonance can be excited due to the periodic structure (Fig. 3.5(b)). We note the two distinct overlapping areas close to reciprocal lattice points $(0, \pm 2\pi / a)$ and $(\pm 2\pi / a, 0)$ in Fig. 3.5(b); these areas correspond to propagating surface plasmon modes confined in the Ag/SiO_2 (substrate) interface in k_y and k_x directions, respectively. Finally, for M_{mag}, the yellow area has overlap with the blue circles in several Brillouin zones, encompassing reciprocal lattice points $(0, \pm 2\pi / a)$, $(\pm 2\pi / a, 0)$, and $(\pm 2\pi / a, \pm 2\pi / a)$, as shown in Fig. 3.5(c). Therefore several branch of plasmon resonances derived from M_{mag} mode can be excited in the periodic fishnet structure.

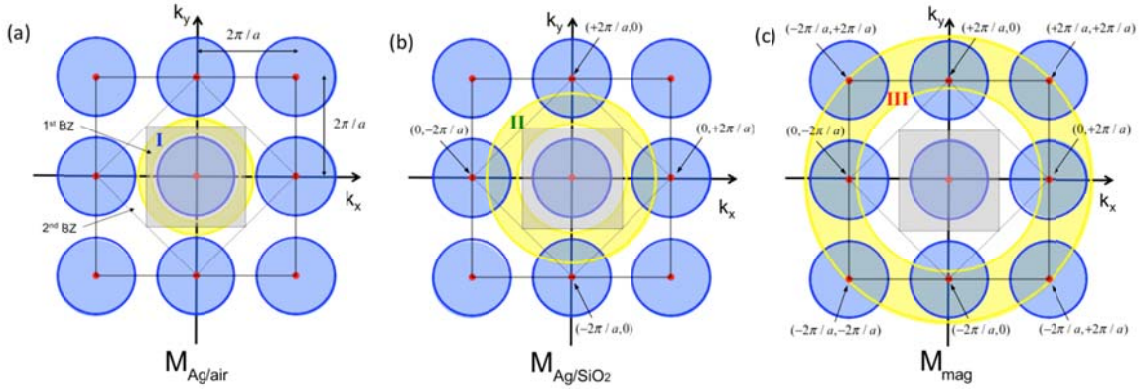

Figure 3.5 Square reciprocal lattice of the infinite film system assuming a periodicity of $a = 600\,\text{nm}$ in $\hat{x}$ and $\hat{y}$ using the extended zone scheme. Blue circle represents the probed k-vector range and encloses each reciprocal lattice point (red dot). Yellow area represents the

dispersion sections I, II, and III in Fig. 3.4(b) for (a) $M_{Ag/air}$, (b) M_{Ag/SiO_2}, and (c) M_{mag}, respectively.

To better understand the multiple resonance branches derived from M_{mag} mode, we examine how the M_{mag} modes of the infinite film system get modified in the fishnet structure due to the fishnet boundary condition, which requires that the electrical current flowing normal to the metal edge to be zero. If the infinite film plasmon mode already (largely) satisfies this boundary condition, it will be a good approximation for the fishnet eigenstate. On the other hand, if the infinite film plasmon mode strongly violates the boundary condition, it will be modified significantly and have a much higher resonance frequency (because the boundary condition often requires extra nodes in the current distribution).

In Fig. 3.6 we plot current distribution of infinite film M_{mag} modes at reciprocal lattice points $(0, \pm 2\pi/a)$, $(\pm 2\pi/a, 0)$, and $(\pm 2\pi/a, \pm 2\pi/a)$. We have chosen symmetric and anti-symmetric combination of these modes, and overlaid the current distribution onto the fishnet structure itself. (Gray and white area represents where the metal and hole of the fishnet would exist.) For convenience we will name these modes for the infinite film system to be $M^{IF}_{m\ o/e,n\ o/e}$, where m and n index the reciprocal lattice points along $\hat{x}$ and $\hat{y}$, and o/e denotes the odd/even symmetry in $\hat{x}$ and $\hat{y}$. The superscript IF refers that they are modes of the infinite film system. For reciprocal lattice points at $(0, \pm 2\pi/a)$, we have two modes $M^{IF}_{0,1o}$ and $M^{IF}_{0,1e}$ with their current distributions shown in Fig. 3.6(a,b). Likewise, for reciprocal lattice points at $(\pm 2\pi/a, 0)$, we have two modes $M^{IF}_{1o,0}$ and $M^{IF}_{1e,0}$ in Fig. 3.6(c,d), and for $(\pm 2\pi/a, \pm 2\pi/a)$ we have $M^{IF}_{1e,1o}$, $M^{IF}_{1o,1o}$, $M^{IF}_{1o,1e}$, and $M^{IF}_{1e,1e}$ as presented in Fig. 3.6(e,f,g,h). We note that $M^{IF}_{1o,0}$ and $M^{IF}_{1e,0}$ correspond to modes along $\hat{x}$, whereas $M^{IF}_{0,1o}$ and $M^{IF}_{0,1e}$ correspond to modes along $\hat{y}$. For the infinite film system, these modes along $\hat{x}$ and $\hat{y}$ are degenerate.

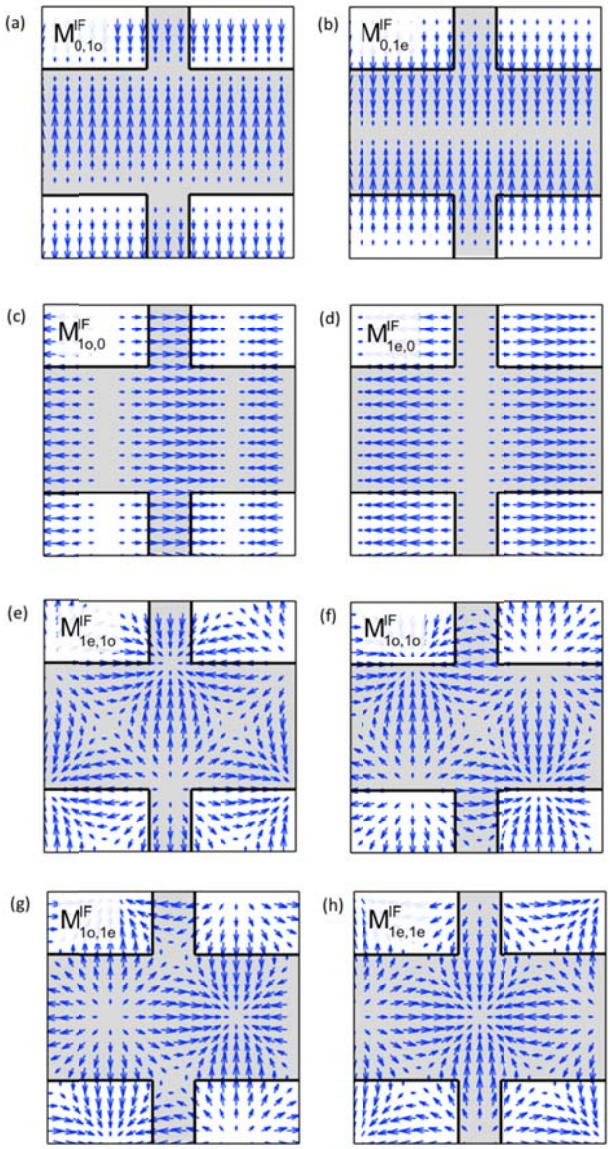

Figure 3.6 Current modes (blue arrows) of the infinite film system at points $(0,1)$, $(1,0)$, and $(1,1)$ as noted in Fig. 3.5(c). (a) $M^{IF}_{0,1o}$ and (b) $M^{IF}_{0,1e}$ are degenerate modes at $(0,1)$. (c) $M^{IF}_{1o,0}$ and (d) $M^{IF}_{1e,0}$ are degenerate modes at $(1,0)$. (e) $M^{IF}_{1e,1o}$, (f) $M^{IF}_{1o,1o}$, (g) $M^{IF}_{1o,1e}$, and (h) $M^{IF}_{1e,1e}$ are degenerate modes at $(1,1)$. The grey area indicates the fishnet geometry for comparison.

Now by examining current distributions of the different modes in Fig. 3. 6, we found that infinite film modes $M^{IF}_{0,1o}$ and $M^{IF}_{1e,1o}$ satisfy the fishnet boundary condition (with no current flowing normal to the position of metal edges) almost perfectly, and modes $M^{IF}_{1o,0}$, $M^{IF}_{1e,0}$, and $M^{IF}_{1o,1o}$ satisfies the fishnet boundary condition reasonably well. Therefore we expect them to be

good approximations to real resonances in the fishnet structure at similar resonance frequencies. Indeed we can identify magnetic plasmon resonances in the fishnet structure with current distribution similar to the infinite film modes $M^{IF}_{0,1o}$, $M^{IF}_{1o,0}$, $M^{IF}_{1e,0}$, $M^{IF}_{1e,1o}$, and $M^{IF}_{1o,1o}$. We display the current distribution of these fishnet eigenmodes in Fig. 3.7, and denote them as $M_{0,1o}$, $M_{1o,0}$, $M_{1e,0}$, $M_{1e,1o}$, and $M_{1o,1o}$. We note that $M_{1o,0}$ and $M_{1e,0}$ are derived from the modes $M^{IF}_{1o,0}$ and $M^{IF}_{1e,0}$ which correspond to modes along $\hat{x}$. The mode $M_{0,1o}$ is derived from $M^{IF}_{0,1o}$ which corresponds to the mode along $\hat{y}$. Unlike the infinite film system, the modes along $\hat{x}$ and $\hat{y}$ for the fishnet are non-degenerate because the wires disrupt the original current distributions; the restoring forces of the charges are changed. This is similar to the behavior in quantum mechanics that when a wavefunction is modified its frequency is shifted. On the other hand, the infinite film modes $M^{IF}_{0,1e}$, $M^{IF}_{1o,1e}$, and $M^{IF}_{1e,1e}$ violates the fishnet boundary condition strongly; there are significant normal current at the metal boundaries which are forced to be cut off and form a node. Thus, these eigenmodes are shifted to much higher energy and is outside our probing range.

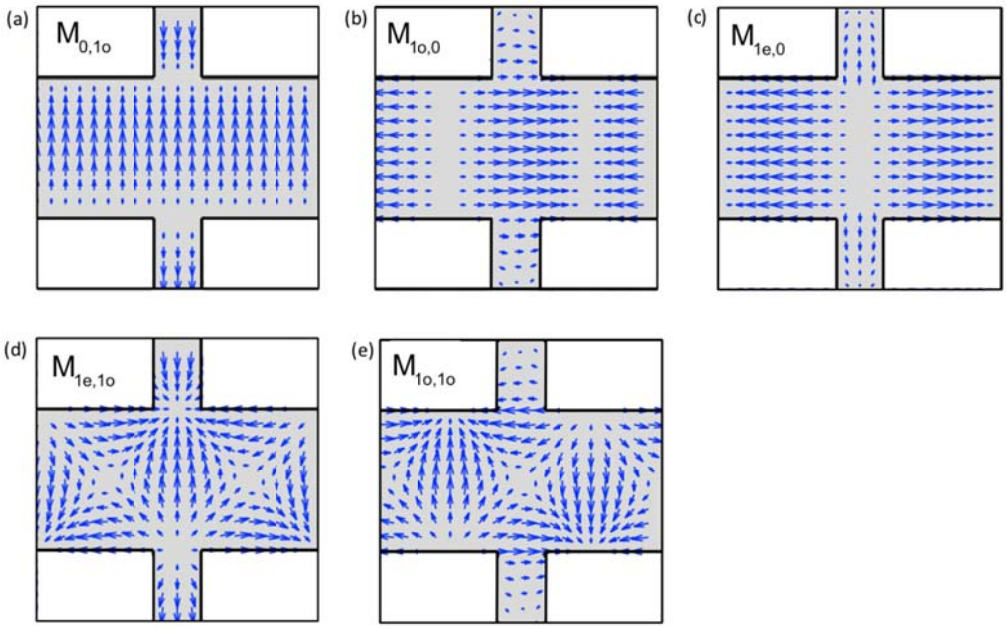

Figure 3.7 The current modes (blue arrows) of the fishnet metamaterial (a) $M_{0,1o}$ (b) $M_{1o,0}$ (c) $M_{1e,0}$ (d) $M_{1e,1o}$ (e) $M_{1o,1o}$.

In summary, we find the modes $M_{0,1o}$, $M_{1o,0}$, $M_{1e,0}$, $M_{1e,1o}$, and $M_{1o,1o}$ to be in our spectral range. These modes are all magnetic resonances at the Γ-point in the folded Brillouin zone, and each anchors a different branch of plasmonic band dispersion. Together with the resonance branch derived from surface plasmon mode M_{Ag/SiO_2}, they form all the observable

resonances in the probed near-infrared spectral range and will be a focus of our discussion. Their excitation strength depends on the incident light polarization and k-vector and will be analyzed in detail in the discussion sections.

3.3.2c Analysis of results and discussion

3.3.2c-1 Plasmon modes in high-symmetry directions ($\phi = 0^\circ$ and 90°)

With the general picture of the plasmon modes of the fishnet in mind, we now analyze the experimental results. The modes in $\phi = 0^\circ$ direction are first investigated. With s-polarized incident light, the electric field is along $\hat{y}$, and the modes $M_{0,1o}$ and $M_{1e,1o}$ with non-zero net-dipole can be excited (Fig. 3.7(a,d)). $M_{0,1o}$ has larger net-dipole than $M_{1e,1o}$ because the oscillating dipole moments of $M_{0,1o}$ are all in-phase along the thick wires. We assign the lower energy resonance R_1^0 as mode $M_{0,1o}$ and the higher energy resonance R_2^0 as mode $M_{1e,1o}$. The excitation strength is consistent with our assignment; R_1^0 is more strongly excited than R_2^0 (Fig. 3.3(a)). The fact that R_2^0 is observed signifies that indeed the thin wires introduce a finite oscillator strength to mode $M_{1e,1o}$. (If the thin wires cease to exist, $M_{1e,1o}$ cannot be excited as the currents in center and boundary of the unit cell perfectly cancel each other; its net-dipole moment becomes zero.)

To support this, we carried out numerical calculations to simulate the optical responses of the fishnet using the finite-element-method (FEM) [76] through COMSOL. In this method, the simulation domain is subdivided into minuscule volumes, i.e., *elements*. Maxwell equations in the form of partial differential equations are solved for each element. The solutions contain the internal field distribution throughout the structure. The fishnet structure illustrated in Fig. 3.1 and appropriate refractive indices for different elements in the structure are used. For silver, we used the optical constants taken from Ref. [77]. The refractive index of the SiO_2 layer is taken to be 1.43. In the calculation, we set the incident light to be normal to the sample with electric field along $\hat{y}$. The results indeed show the two resonant modes $M_{0,1o}$ and $M_{1e,1o}$ as presented in Fig. 3.8. Mode $M_{1o,1o}$ is unobserved because currents in the thick wires of a unit cell cancel each other and its net-dipole is zero.

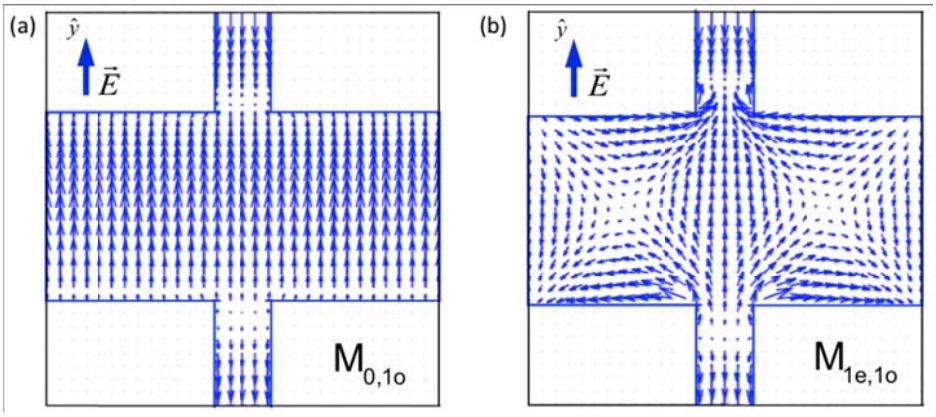

Figure 3.8 Numerically calculated current distributions showing the modes corresponding to (a) $M_{0,1o}$ (b) $M_{1e,1o}$. The incident electric field polarization is along $\hat{y}$.

The dispersion of R_1^0 and R_2^0 are plotted in Fig. 3.9. They exhibit positive and negative dispersion, respectively. This is because with increasing k_t, the mode distribution of R_1^0 evolves into that of the higher energy R_2^0. This can be seen by comparing $M_{0,1o}$ and $M_{1e,1o}$ in Fig. 3.7(a,d). With increasing k_t, currents of $M_{0,1o}$ in the center and boundary of the unit cell become more out-of-phase like that of $M_{1e,1o}$. On the other hand, currents of $M_{1e,1o}$ in the center and boundary of the unit cell become more in-phase like that of $M_{0,1o}$. Thus, the current distribution of R_1^0 becomes more like the higher energy mode R_2^0 and exhibits positive dispersion. Likewise, R_2^0 exhibits negative dispersion as its current distribution becomes more like the lower energy mode R_1^0. We can picture that the positive band of R_1^0 is folded back from the BZ edge to the zone center. This folded back band corresponds to the negative dispersion of mode R_2^0. We also observe that the mode strength of R_1^0 decreases whereas R_2^0 increases in Fig. 3.3(a). Similar to the dispersion, this can be explained from the variation of the current distribution of $M_{0,1o}$ and $M_{1e,1o}$ in Fig. 3.7(a,d). For $M_{0,1o}$, the net-dipole decreases as the currents in the center and boundary become out-of-phase with increasing k_t. On the other hand, for $M_{1e,1o}$, the net-dipole increases as the dipoles in the center and boundary are initially out-of-phase but become more in-phase with increasing k_t. From this picture, we can understand that the initially bright R_1^0 becomes darker and the dark R_2^0 becomes brighter.

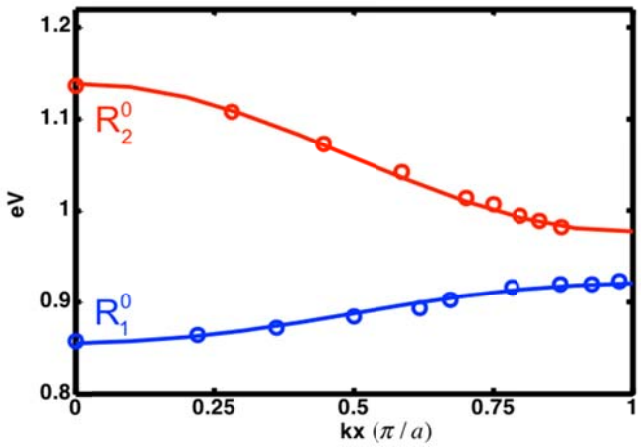

Figure 3.9 Experimentally measured plasmon modes R_1^0 (blue) and R_2^0 (red) as a function of k_t in the direction of $\phi = 0^\circ$. R_1^0 and R_2^0 exhibit positive and negative dispersion, respectively.

Next, we investigate the plasmon modes in the $\phi = 90^\circ$ direction along $\hat{y}$. With p-polarized incident light, the y-z plane has mirror symmetry and only even modes with respect to this mirror plane, i.e., $M_{0,1o}$, $M_{1e,1o}$, and $M_{1e,0}$, can be excited. As we have discussed earlier, $M_{0,1o}$ has larger net-dipole than $M_{1e,1o}$ due to its in-phase currents along the thick wires. $M_{1e,0}$ is forbidden at normal incidence but allowed with finite k_t due to the phase variations in the thin wires (Fig. 3.7(c)). We assign R_1^{90}, R_2^{90}, and R_3^{90} to be $M_{0,1o}$, $M_{1e,1o}$, and $M_{1e,0}$, respectively. Consistent with our assignments, in Fig. 3.3(b), we observe R_1^{90} to be strongest and R_3^{90} is unobserved at normal incidence but appears at finite k_t. In addition, we observe the mode R_{Ag/SiO_2}^{90} in Fig. 3.3(b) and assign it to be M_{Ag/SiO_2} at finite k_t. To understand this, we plot the measured dispersion of R_{Ag/SiO_2}^{90} as green circles in Fig. 3.10 after calculating its k-vector using the relation $-k_{in} + 2\pi / a = k_t$. (k_{in} is the tangential k-vector of the incident photon.) The blue line corresponds to the dispersion of M_{Ag/SiO_2} as calculated for the infinite film system. We see that they match well confirming our assignment of R_{Ag/SiO_2}^{90} to the mode M_{Ag/SiO_2}. The deviation at higher energies can be understood as the band lowering effect near $k_t = 2\pi / a$.

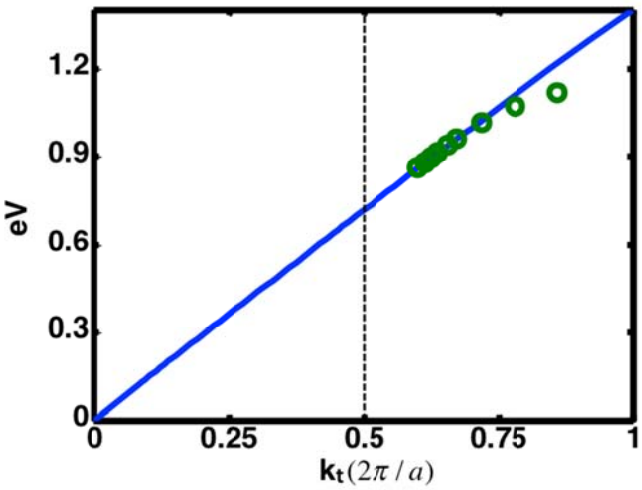

Figure 3.10 Experimentally measured dispersion of R^{90}_{Ag/SiO_2} (green circles) and the calculated dispersion of mode M_{Ag/SiO_2} of the infinite thin film system (blue line).

To support our assignments, we carried out numerical calculation in this direction with p-polarized light. At normal incidence, we confirm that R^{90}_1 and R^{90}_2 correspond to $M_{0,1o}$ and $M_{1e,1o}$, respectively. (Field distribution is same as shown in Fig. 3.8.) The field distribution of R^{90}_3 with $\theta_{in} = 10^\circ$ is present in Fig. 3.11(a). With the currents of thick and thin wires all pointing away from the center of unit cell, we confirm that R^{90}_3 conforms to mode $M_{1e,0}$ as depicted in Fig. 3.7(c). Finally, Fig. 3.11(b) shows the field distribution of R^{90}_{Ag/SiO_2} at $\theta_{in} = 10^\circ$ corresponding to surface plasmon modes with large normal component.

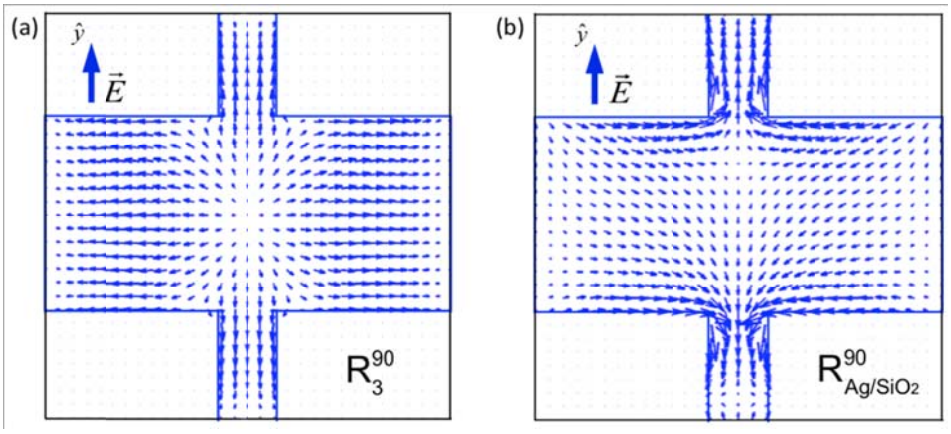

Figure 3.11 Numerically calculated current distribution of (a) R^{90}_3 and (b) R^{90}_{Ag/SiO_2} for $\phi = 90^\circ$ at $\theta_{in} = 0^\circ$. They correspond to $M_{1e,0}$ and M_{Ag/SiO_2}, respectively. The incident electric field polarization is along $\hat{y}$.

In Fig. 3.3(b), we observe the mode strength of R_1^{90} becomes weaker with increasing k_t. This can be understood from the fact that the $\hat{y}$ component of the incident electric field (E_y), being the tangential field, is responsible for exciting $M_{0,1o}$ in Fig. 3.7(a). In the experiment, as the incident light is p-polarized, the tangential component (E_y) decreases while the normal component (E_z) increases with larger θ_{in}. Hence, the excitation of $M_{0,1o}$ is reduced and correspondingly R_1^{90} becomes weaker. The situation is similar with R_2^{90}. It becomes weaker due to decreasing E_y. Mode R_3^{90} is unobserved at normal incidence but appears at finite k_t. This is because its excitation is forbidden due to its net-zero dipole moment at normal incidence (see mode $M_{1e,0}$ in Fig. 3. 7(c)). However, with finite k_t, the phase variation in the thin wires prevents their cancelation in the unit cell and induces a stronger mode strength. Lastly, we observe in Fig. 3.3(b) that R_{Ag/SiO_2}^{90} exhibits a stronger dip of T and peak of R as θ_{in} increases. The spectra of A also show resonance but it is more pronounced in T and R because resonances with very large dipole moment have the effective radiation damping to be much larger than absorption damping. These pronounced spectral features are similar to that shown in systems such as corrugated dielectric waveguides [78]. With increasing θ_{in}, the features of T and R become more pronounced because surface plasmon polaritons have a large normal field component and its coupling with incident light becomes stronger due to the increasing E_z field.

3.3.2c-2 Plasmon modes in low-symmetry directions ($\phi = 22.5^\circ, 45^\circ,$ and 67.5°)

In this section, we investigate the plasmon modes in $\phi = 22.5^\circ, 45^\circ,$ and 67.5° directions. We first focus on the normal incidence case where only $M_{0,1o}$, $M_{1e,1o}$, and $M_{1o,0}$ can be excited due to the presence of x-z and y-z mirror planes. $M_{0,1o}$ has largest net-dipole moment whereas $M_{1o,0}$ has the weakest (see Fig. 3.7(a,b,d)). At $\theta_{in} = 0^\circ$, Fig. 3.3(c,d,e) shows that only two modes R_{1A}^{ϕ} and R_2^{ϕ} are observed. (Here, we refer $\phi = 22.5,\ 45,$ and 67.5.) Their positions correspond to the $k_t = 0$ energy positions of R_1^0 and R_2^0 (or R_1^{90} and R_2^{90}) at 0.85eV and 1.14eV, respectively. Therefore, we assign R_{1A}^{ϕ} as mode $M_{0,1o}$ and R_2^{ϕ} as $M_{1e,1o}$ for $k_t = 0$. However, the mode $M_{1o,0}$ is unobserved in our linear spectra. To understand this, we carried out numerical calculations with electric field along $\hat{x}$ at normal incidence for a detailed analysis. In this case, only mode $M_{1o,0}$ can be excited due to the x-z mirror plane (Fig. 3.7). From our results, although no clear feature is discernible in the linear spectra, we confirm a resonant mode with a field distribution as Fig. 3.12(a) lying 50meV above $M_{0,1o}$. This mode conforms to $M_{1o,0}$ as the currents on the center and boundary of the unit cell are out-of-phase as

depicted in Fig. 3.7(b). We find that the electric field amplitude of this resonance is 20 times smaller than that of the background electric field (Fig. 3.12(b)). (The background electric field is from the tail of the mode at zero-frequency.) As absorption is proportional to intensity, the absorption due to the electric field of the resonant mode is 400 times smaller than the absorption due to background electric field. This is because the oscillator strength of $M_{1o,0}$ is very weak as its dipole moment is close to zero. (In fact, without the thin wires it has non-zero dipole moment; the difference of the currents in the junction and non-junction prevent it to be zero.)

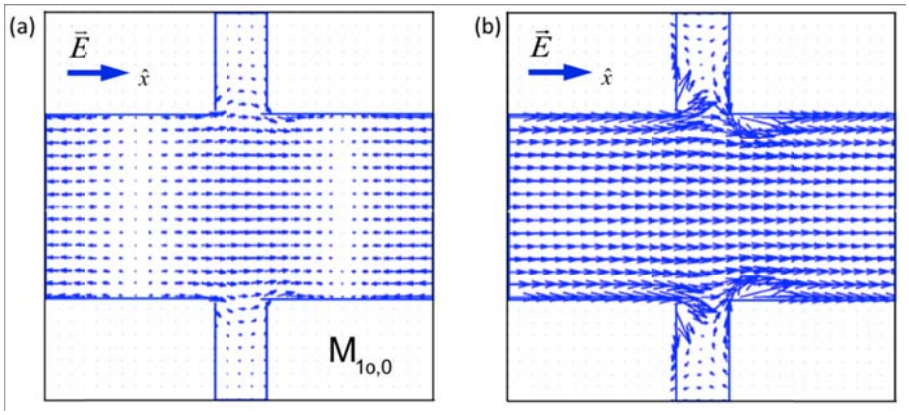

Figure 3.12 Numerically calculated current distributions showing the modes corresponding to (a) $M_{1o,0}$ (b) background current. The incident electric field polarization is along $\hat{x}$.

Interestingly, R_{1A}^{ϕ} initially shifts to higher energy but then shifts to lower energy when R_{1B}^{ϕ} starts to appear. The dash lines in Fig. 3.3(c,d,e) illustrate this change in shift direction. Thus, R_{1A}^{ϕ} and R_{1B}^{ϕ} appear to be splitting from each other with increasing k_t. This kind of avoid-crossing behavior is observed in quantum systems. We understand this plasmon dispersion behavior as the following discussion.

In our numerical calculation, we observed two modes $M_{0,1o}$ and $M_{1o,0}$ with the latter being 50meV higher in energy. These two modes lying close to each other can couple when their modes are not orthogonal. Since, $M_{1o,0}$ is a weaker mode, its coupling to the stronger $M_{1o,0}$ mode will allow it to become observable. The coupling will only be allowed when the two modes are not orthogonal and this depends on the direction of k_t. Thus, we assign R_{1A}^{ϕ} and R_{1B}^{ϕ} to be the coupled modes of $M_{0,1o}$ and $M_{1o,0}$. In the following, we show that the coupling is allowed only for low-symmetry directions and that our observation is consistent with this picture.

First, we discuss the coupling at normal incidence ($\theta_{in} = 0^\circ$). Coupling between two modes depend on their mode overlap and is determined by

$$\int \vec{E}(\vec{r}) \cdot \vec{p}(\vec{r})\, d\vec{r} \tag{3.2}$$

where $\vec{E}(\vec{r})$ is the electric field of one mode and $\vec{p}(\vec{r})$ is the dipole of the other mode. For $k_t = 0$, Eq. (3.2) is zero because of the symmetric distribution of $\vec{E}(\vec{r})$ and $\vec{p}(\vec{r})$ with respect to x-z and y-z mirror planes (Fig. 3.13(a)). Therefore, the two modes are orthogonal and no coupling occurs and this is consistent with that we only observe one mode for $k_t = 0$.

Second, we consider the coupling in the directions of $\phi = 0^\circ$ and 90°. Fig. 3.13(b) illustrates the modes with a finite $\vec{k}_x$ ($\phi = 0^\circ$); the phase is varying in $\hat{x}$. Here, Eq. (3.2) is again zero because of the mirror symmetry in the x-z plane; the integration at $\vec{r} = (x, y, z)$ is canceled by that of the position $\vec{r}\,' = (x, -y, z)$. Fig. 3.13(c) depicts the modes with a finite $\vec{k}_y$ ($\phi = 90^\circ$) Similarly, the mode overlap is zero due to the mirror symmetry in the y-z plane; the integration at $\vec{r} = (x, y, z)$ is canceled by that of the position $\vec{r}\,' = (-x, y, z)$. Therefore, it is clear that the coupling of $\mathsf{M}_{0,1o}$ and $\mathsf{M}_{1o,0}$ is forbidden in the directions of $\phi = 0^\circ$ and 90° and again consistent with our experimental observations.

Third, the coupling in the directions of $\phi =$ 22.5°, 45°, and 67.5° is considered. A finite $\vec{k}_t$ induces phase variations in both $\hat{x}$ and $\hat{y}$ as depicted in Fig. 3.13(d). Due to the phase variation, no mirror planes exist. Eq. (3.2) ceases to be zero as k_t becomes finite. Therefore, coupling between $\mathsf{M}_{0,1o}$ and $\mathsf{M}_{1o,0}$ are allowed and become stronger with increasing k_t. The coupling mixes the bright and dark mode making the latter to become visible. This is the reason we observe the coupling behavior of R^{ϕ}_{1A} and R^{ϕ}_{1B} in low-symmetry directions (Fig. 3.3(c,d,e)).

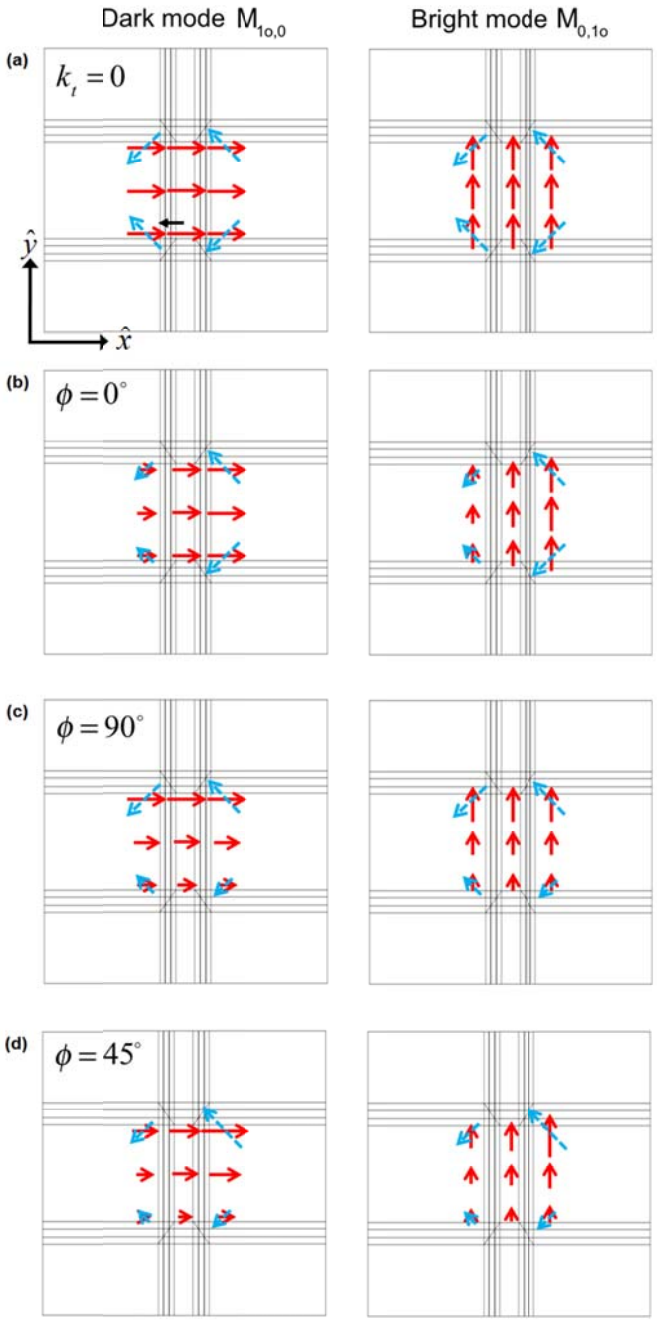

Figure 3.13 Illustration of the mode overlap between the dark mode ($M_{1o,0}$) and bright mode $M_{0,1o}$ for (a) $k_t = 0$ (b) $\phi = 0^\circ$ (c) $\phi = 90^\circ$ (d) $\phi = 45^\circ$. Red arrows indicate the induced dipoles of $M_{1o,0}$ (left) and $M_{0,1o}$ (right). Blue dashed arrows is a schematic representation of the electric field distribution by the dark mode ($M_{1o,0}$).

We further analyze the coupling of the bright mode ($\mathsf{M}_{0,1o}$) and dark mode ($\mathsf{M}_{1o,0}$) and deduce the dispersion of the latter from our experimental results. Particularly, we focus on $\phi = 45^\circ$ but the discussion is also applicable to $\phi = 22.5^\circ$ and 67.5°. Fig. 3.14(a) plots the dispersion of R_{1A}^{45} and R_{1B}^{45} (red circles) as observed in Fig. 3.3(d). In experiment, we can only observe the coupled modes. We also know the dispersion of the uncoupled bright mode from our measurements in $\vec{k}_t = \vec{k}_x$ and $\vec{k}_t = \vec{k}_y$. With this information, we predict the dispersion of the dark mode where the coupled modes can be explicitly expressed in terms of the uncoupled modes. We denote the dark mode and bright mode as eigenstates ϕ_d and ϕ_b, respectively. Their energy eigenvalues are E_d and E_b prior to coupling. When the two states are allowed to interact, the eigenstates become a linear combination of ϕ_d and ϕ_b, and to find their energy we must find the eigenvalues of the matrix

$$\begin{pmatrix} E_d & H_{\text{int}} \\ H_{\text{int}} & E_b \end{pmatrix} \tag{3.3}$$

where H_{int} is the coupling coefficient [79]. The eigenvalues are

$$E_{\pm} = \frac{E_d + E_b}{2} \pm \sqrt{H_{\text{int}}^2 + \Delta^2} \tag{3.4}$$

where $\Delta = \frac{|E_d - E_b|}{2}$ is half of the energy separation between ϕ_d and ϕ_b. The new eigenstates are a linear combination of ϕ_d and ϕ_b and given as

$$\begin{aligned} \phi_+ &= a_+\phi_d + b_+\phi_b \\ \phi_- &= a_-\phi_d + b_-\phi_b \end{aligned} \tag{3.5}$$

where $a_+ = -\frac{\Delta - \sqrt{H_{\text{int}}^2 + \Delta^2}}{H_{\text{int}}}$, $b_+ = 1$, $a_- = 1$, and $b_- = -\frac{H_{\text{int}}}{\Delta + \sqrt{H_{\text{int}}^2 + \Delta^2}}$. In Fig. 3.14(a), the upper and lower red circles corresponds to ϕ_+ and ϕ_-, respectively. The blue solid curve corresponds to ϕ_b. Using Eq. (3.4), we calculated the dispersion of ϕ_d and presented as the black solid curve. Furthermore, Fig. 3.14(b) shows the calculated dispersion of H_{int}. It clearly shows that the coupling becomes stronger with increasing $\vec{k}_t$ as we have discussed previously. Fig. 3.14(c) shows the normalized coefficients a_+ and b_+ for ϕ_+. We confirm that ϕ_+ is purely a dark mode at $k_t = 0$ and the contribution of the bright mode becomes larger with increasing k_t. ϕ_- shows similar behavior with the contribution of the dark and bright modes reversed.

This also explains the change of the mode strength of R^{ϕ}_{1A} and R^{ϕ}_{1B} in Fig. 3.3(c,d,e). The increased contribution of the dark $M_{1o,0}$ to R^{ϕ}_{1A} makes it weaker whereas the increased contribution of $M_{0,1o}$ to R^{ϕ}_{1B} makes it stronger and visible at finite k_t.

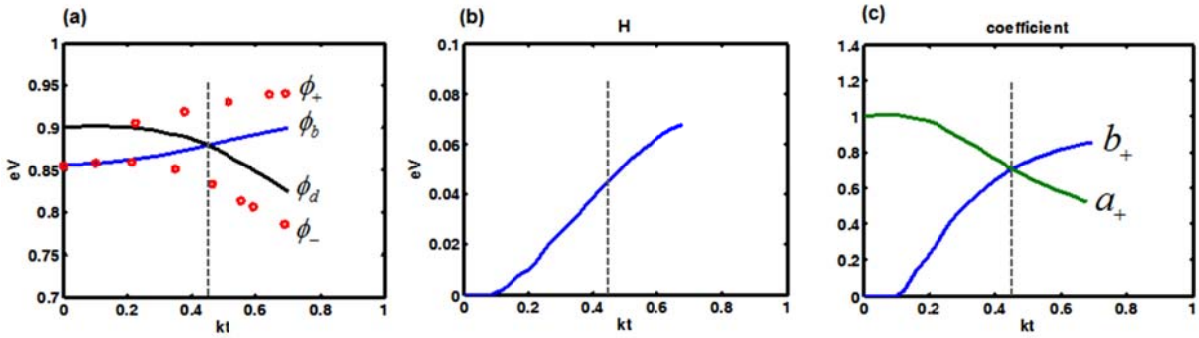

Figure 3.14 Coupling behavior of R^{45}_{1A} and R^{45}_{1B}: (a) Dispersion of the uncoupled (ϕ_d, ϕ_b) and coupled modes (ϕ_+, ϕ_-). The red circles and blue solid line are from experimental results and the black solid line is calculated from Eq. (3.4); (b) Dispersion of the coupling coefficient H_{int}; (c) Normalized amplitude of the dark (a_+) and bright (b_+) mode contributing to ϕ_+.

3.3.2-d Relation of observed modes to the general modes of fishnet

In the experiment, the observed six modes are labeled as R^{ϕ}_1, R^{ϕ}_2, R^{ϕ}_{1A}, R^{ϕ}_{1B}, R^{ϕ}_3, and R^{ϕ}_{Ag/SiO_2} depending on ϕ. In the general picture, we discussed that the modes $M_{0,1o}$, $M_{1o,0}$, $M_{1e,0}$, $M_{1e,1o}$, $M_{1o,1o}$, and M_{Ag/SiO_2} are expected to be observed. From our analysis, we find that R^{ϕ}_1 and R^{ϕ}_2 correspond to $M_{0,1o}$ and $M_{1e,1o}$, respectively. Modes R^{ϕ}_{1A} and R^{ϕ}_{1B} are mixed modes of $M_{0,1o}$ and $M_{1o,0}$. Mode R^{ϕ}_3 corresponds to $M_{1e,0}$, and R^{90}_{Ag/SiO_2} to M_{Ag/SiO_2}. Thus, the measured six modes are related to the five distinct modes $M_{0,1o}$, $M_{1o,0}$, $M_{1e,0}$, $M_{1e,1o}$, and M_{Ag/SiO_2}. In our measurements, we are unable to observe $M_{1o,1o}$ because it is a dark mode (Fig. 3.7(e)) where its current oscillations are perfectly canceled in the unit cell.

3.4 k-dependent effective optical constants

In a natural material, the optical constants, i.e., n, z, ε, and μ, are useful in describing its material properties. Likewise, *effective* optical constants can be informative in understanding the characteristics of a metamaterial structure. In practice, these can be deduced from the complex transmission and reflection coefficients. In this section, we carry out phase measurements using an interferometric setup and deduce the k-dependent effective optical

constants for the first time. The retrieval procedure is presented and then the experiment results are discussed.

3.5 Retrieval procedure

We briefly describe the formalism to retrieve the k-dependent effective optical constants from the measured transmission ($\hat{t}$) and reflection ($\hat{r}$) coefficients. Here, it is assumed that the metamaterial is a homogenous slab of thickness d with its normal pointing in z direction (Fig. 3.15). Furthermore, the metamaterial is considered to have mirror symmetry in the x-z and y-z plane. Thus, the effective material tensors of the slab can be expressed in the form of

$$\vec{\varepsilon} = \begin{pmatrix} \varepsilon_{xx} & 0 & 0 \\ 0 & \varepsilon_{yy} & 0 \\ 0 & 0 & \varepsilon_{zz} \end{pmatrix} \text{ and } \vec{\mu} = \begin{pmatrix} \mu_{xx} & 0 & 0 \\ 0 & \mu_{yy} & 0 \\ 0 & 0 & \mu_{zz} \end{pmatrix}. \tag{3.6}$$

This is true for the fishnet as well as for many other proposed metamaterial structures. As shown in Fig. 3.15, the front and back semi-infinite medium is considered to be medium 1 and medium 3 with isotropic material properties (ε_1, μ_1) and (ε_3, μ_3), respectively.

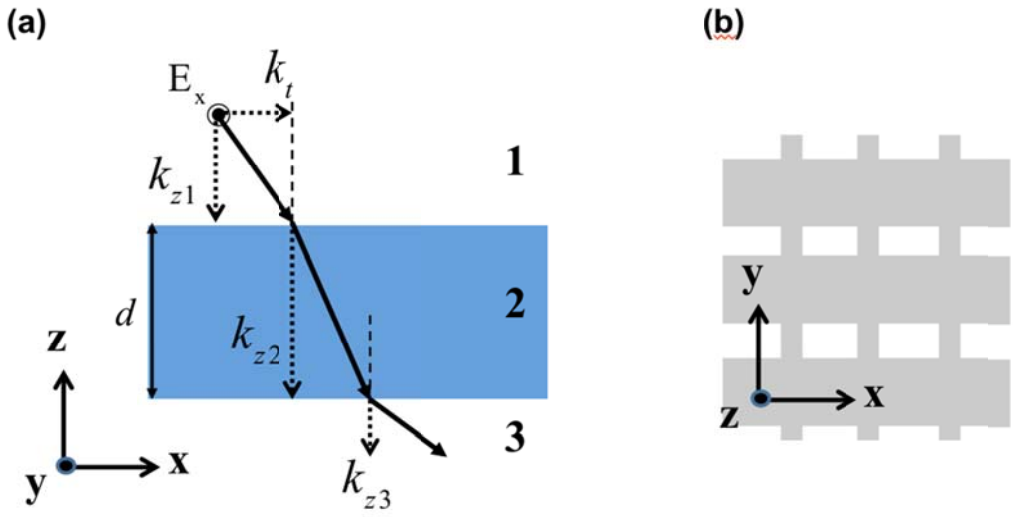

Figure 3.15 Beam geometry of incident s-polarized light on x-z plane. (a) Metamaterial slab (medium 2) with thickness d between semi-infinite medium 1 (front) and medium 3 (back). The electric field is along y direction. (b) Top view of fishnet showing x-z and y-z symmetry planes.

The beam geometry is depicted in Fig. 3.15. The light is incident on the x-z plane from medium 1. In the experiment, the light is s-polarized with electric field along y in order to excite the magnetic resonance with currents perpendicular to the thick wires. Thus, the electric field has y component and magnetic field has x and z components. The normal wavevector for each medium are k_{z1}, k_{z2}, and k_{z3} as illustrated in Fig. 3.15(a). The tangential wavevector is $k_t = \sqrt{\varepsilon_1 \mu_1}\sin\theta_1$ in all medium. With this geometry, the transmission and reflection coefficients can be expressed in terms of the angle-dependent wavevectors in medium 1, 2, and 3 as

$$\hat{t} = \frac{2k_{z1}\dfrac{k_{z2}}{\mu_{xx}}}{\dfrac{k_{z2}}{\mu_{xx}}(k_{z1}+k_{z3})\cos(k_{z2}d) - i\left(\dfrac{k_{z2}^2}{\mu_{xx}^2}+k_{z1}k_{z3}\right)\sin(k_{z2}d)} \tag{3.7}$$

$$\hat{r} = \frac{\dfrac{k_z}{\mu_{xx}}(k_{z1}-k_{z3})\cos(k_{z2}d) + i\left(\dfrac{k_{z2}^2}{\mu_{xx}^2}-k_{z1}k_{z3}\right)\sin(k_{z2}d)}{\dfrac{k_{z2}}{\mu_{xx}}(k_{z1}+k_{z3})\cos(k_{z2}d) - i\left(\dfrac{k_{z2}^2}{\mu_{xx}^2}+k_{z1}k_{z3}\right)\sin(k_{z2}d)}$$

where $k_{z1} = \sqrt{k_o^2\varepsilon_1\mu_1 - k_t^2}$, $k_{z3} = \sqrt{k_o^2\varepsilon_3\mu_3 - k_t^2}$, and

$$k_{z2} = \sqrt{k_o^2\varepsilon_{yy}\mu_{xx} - k_t^2\mu_{xx}/\mu_{zz}}\,.$$

(3.8)

Eq. (3.7) can be inverted to relate the material parameters of medium 2 with $\hat{t}$ and $\hat{r}$ as,

$$k_{z2}d = \pm\cos^{-1}\left(\frac{k_{z1}(1-\hat{r}^2)+k_{z3}\hat{t}^2)}{\hat{t}[k_{z1}(1-\hat{r})+k_{z3}(1+\hat{r})]}\right),$$

(9)

$$\frac{k_{z2}}{\mu_{xx}} = \pm\sqrt{\frac{k_{z1}^2(\hat{r}^2-1)-k_{z3}^2\hat{t}^2}{1+\hat{r}^2-\hat{t}^2}}\,.$$

(3.10)

Furthermore, the effective index of the metamaterial slab can be obtained from

$$n = \pm\sqrt{k_{z2}^2+k_t^2}\,/\,k_o\,.$$

(3.11)

From Eqs. (3.8-11), n, ε_{yy}, and μ_{xx} is obtained upon assuming the normal component $\mu_{zz}=1$ with no resonance. Similar relations can be obtained for p-polarized incident light giving the expressions for ε_{xx} and μ_{yy}. Here, we focus on obtaining μ_{xx} using s-polarized light as it contains the information of the excited magnetic resonance.

3.4.2 Experimental scheme

We carry out phase measurements of the complex transmission ($\hat{t}$) and reflection ($\hat{r}$) coefficients using the setup depicted in Fig. 3.16 which implements a Newton interferometer arrangement. The light source was the super-continuum fiber laser described in previous sections. A 2D InGaAs CCD camera was used to detect the interference fringe due to the overlap of the sample and reference images. The absolute phase is deduced by comparing the fringes in the substrate and fishnet (Fig. 3.16 inset).

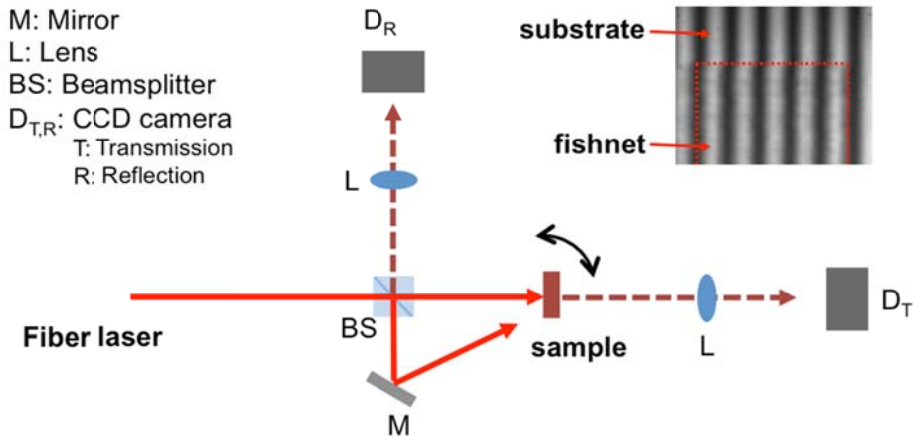

Figure 3.16 Experimental setup to measure the phase of transmitted and reflected light. Near-infrared tunable pulses are provided by a super-continuum fiber laser. The interference pattern is detected by an InGaAs CCD camera. The absolute phase is obtained by compared the fringe on the substrate and fishnet (inset).

3.4.3 Results and discussion

We focus on characterizing the lower energy magnetic resonance for $\phi = 0^\circ$ using s-polarized light. Fig. 3.17 display the measured $T=|\hat{t}|^2$, $R=|\hat{r}|^2$, ϕ_t, and ϕ_r. The magnetic resonance with its characteristic features is identified around 0.85eV. We note the dip of T is associated with the curvature variation, i.e., kink behavior, of ϕ_t (Fig. 3.17(a,c)). This can be understood from Kramers-Kronig relations where it is known that the phase is related to the slope of amplitude [80]. The dip in T has its slope varying from negative to positive and is correlated as a kink behavior in ϕ_t. For R, the slope doesn't exhibit a change of sign and the spectra of ϕ_r have monotonous dispersion (Fig. 3.17(b,d)). The effective n, ε_{yy}, μ_{xx}, and their k-dependent spectra are deduced and are plotted in Fig. 3.18. The spectra of μ_{xx} shows a prominent resonant feature whereas ε_{yy} exhibits a monotonous plasma dispersion. This confirms that the resonance is strongly magnetic. The structural parameters of the fabricated fishnet do not give negative values for the real part of μ_{xx}. However, the real part of n is

negative as the condition $\mathrm{Re}(\varepsilon_{xx})\,\mathrm{Im}(\mu_{yy}) + \mathrm{Re}(\mu_{yy})\,\mathrm{Im}(\varepsilon_{xx}) < 0$ to achieve negative index is satisfied [47]. Thus, the negative refraction is mainly due to the real part of ε_{yy} and imaginary part of μ_{yy} as has been observed in other studies [17, 64, 81, 82]. The resonant position of μ_{xx} is observed to shift to higher energy with increasing k_t. Spectral changes in the transmission and reflection are associated with this shift. This indicates that the dispersion of the magnetic resonance is responsible for the observed changes. Thus, we experimentally confirm that the resonance is magnetic in nature and the observed dispersion is due to the shift of the magnetic resonance.

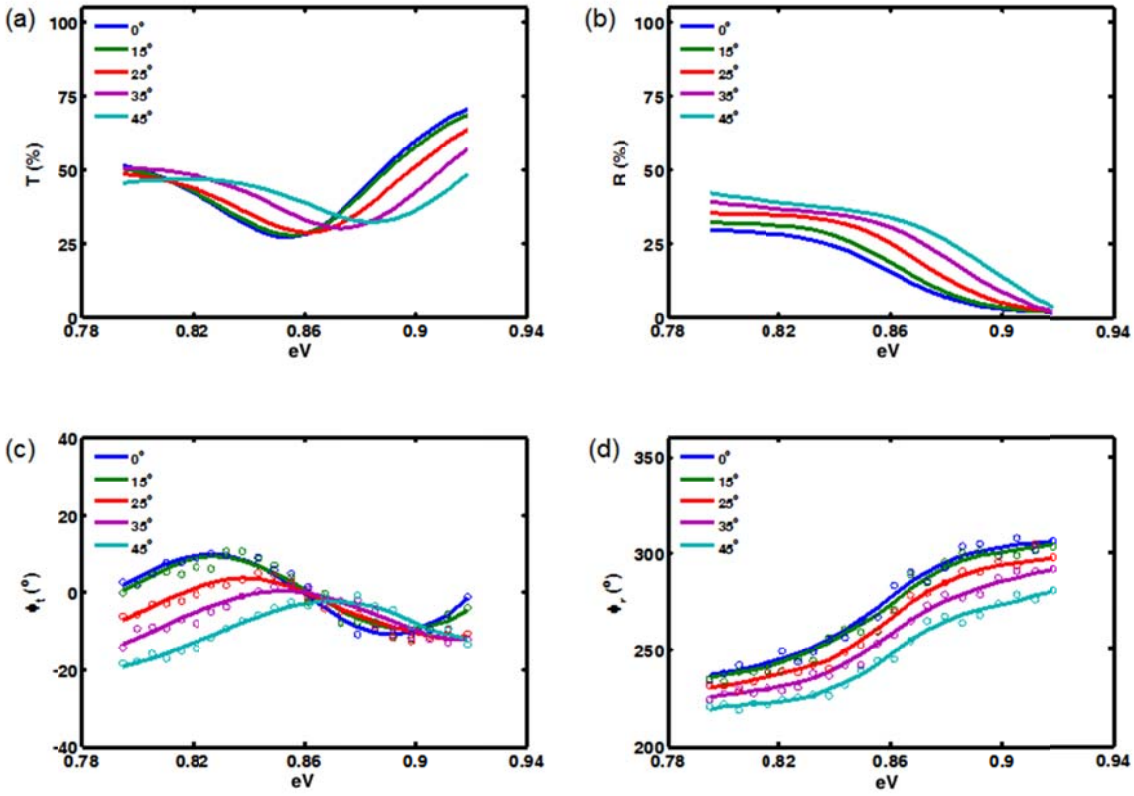

Figure 3.17 Experimentally measured angle-dependent spectra of (a) T (b) R (c) ϕ_t (d) ϕ_r.

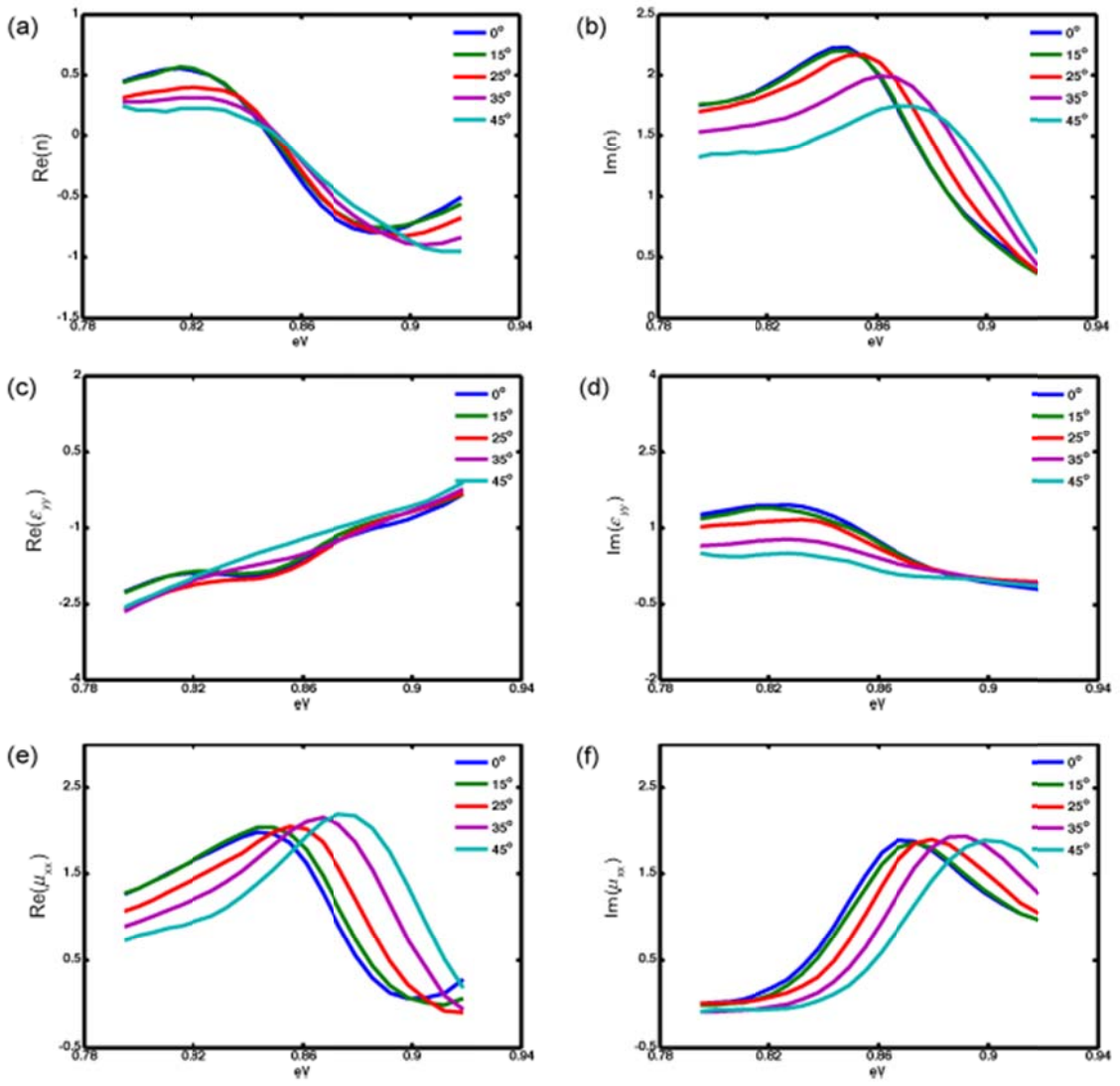

Figure 3.18 Experimentally measured angle-dependent spectra of n, ε_{yy}, and μ_{xx} deduced from Eqs. (3.8-11); (a) Re(n) (b) Im(n) (c) Re(ε_{yy}) (d) Im(ε_{yy}) (e) Re(μ_{xx}) (f) Im(μ_{yy}).

3.5 Conclusions

In summary, we probed the plasmon band structure of the fishnet metamaterial using angle- and polarization- resolved spectroscopy. Multiple magnetic bands are shown to exist in the near-infrared spectral range. Most interestingly, we identify dark modes that couple strongly with the bright magnetic modes in low-symmetry directions. This leads to hybridization of the bands accompanied with avoid-crossing behavior. Such effects are analogous to the mixing of extended electronics states in solids and should be considered in designing metamaterials. In addition, we develop a phase measurement technique and measure

the k-dependent effective optical constants for the first time. We show that plasmon dispersion originates from the shift of the magnetic resonance in the effective permeability. Our approach sets up a basis for characterizing the plasmon band structure of other metamaterials.

Chapter 4

Second harmonic generation in optical metamaterials

4.1 Motivation

In recent years, there have been a number of reports on studies of nonlinear optical properties of metamaterials. The first attempts were mainly theoretical; experimental works appeared only recently. Pendry [10] suggested that enhanced nonlinear optical responses could be observed in metamaterials composed of split ring resonators (SRR) at the magnetic resonance. A series of experiments showed significantly enhanced second-harmonic generation (SHG) from gold SRRs arrays at their magnetic resonance frequencies [12, 83, 84], but the signals were obtained at a single frequency. Later, it was observed that SHG from a fishnet metamaterial exhibited strong enhancement at the magnetic resonance [85]. It was suggested that unlike in a molecular system, the resonant enhancement came from local-field enhancement through the excitation of the plasmon resonance. However, detailed comparison of experimental results with theoretical calculation has not been done and quantitative understanding of the observations has been limited.

In this chapter, we experimentally study the nonlinear response of a fishnet structure with $Ag/SiO_2/Ag$ sandwiched layers using second harmonic generation (SHG) spectroscopy. Also, the SHG response from the metamaterial was theoretically calculated. The approach combines finite-difference-time-domain (FDTD) simulation with a field integration technique. The calculated SHG spectra around the magnetic resonance show quantitative agreement with the experimentally measured spectra of P and S polarization combinations. The maximum resonance enhancement of SHG reaches ~80 times of that from a flat Ag surface for the P-in/P-out polarization combination, suggesting that metamaterials could be potentially useful as nonlinear optical materials in some applications. Furthermore, the theoretical calculations are able to explain many interesting features observed in experiment, and allow design of structure that maximizes SHG.

4.2 Second harmonic generation spectroscopy

The basic theory of SH spectroscopy is well established [86], and only a brief introduction is presented here. When an electric field $\vec{E}(\omega)$ is incident on a medium, a second order nonlinear polarization $\vec{P}(2\omega)$ is induced. Under the electro-dipole approximation it is express as

$$\vec{P}(2\omega) = \varepsilon_0 \vec{\vec{\chi}}^{(2)}_{eee} : \vec{E}(\omega)\vec{E}(\omega) \tag{4.1}$$

where $\vec{\vec{\chi}}^{(2)}_{eee}$ is the electro-dipole contribution to the second-order nonlinear susceptibility tensor. $\vec{P}(2\omega)$ generates a signal at 2ω and its intensity has a quadratic dependence to the effective nonlinear susceptibility $\vec{\vec{\chi}}^{(2)}_{eff}$. For a plane wave input, the SH signal is expressed as

$$I(2\omega) = \frac{\omega^2 \mid \vec{\vec{\chi}}^{(2)}_{eff} \mid^2 I^2(\omega)}{8\varepsilon_0 c^3 \cos^2\beta} \tag{4.2}$$

where $I(\omega)$ is the input intensity and β is the exit angle of 2ω with respect to surface normal. The effective nonlinear susceptibility has the form

$$\vec{\vec{\chi}}^{(2)}_{eff} = [\vec{\vec{L}}(2\omega)\cdot\hat{e}_{2\omega}]\cdot\vec{\vec{\chi}}^{(2)} : [\vec{\vec{L}}(\omega)\hat{e}_{\omega}][\vec{\vec{L}}(\omega)\hat{e}_{\omega}] \tag{4.3}$$

where $\hat{e}_i$ is the unit vector of the polarization of $\vec{E}$ field and $\vec{\vec{L}}$ being the tensorial Fresnel factor. In our experiment, we use the geometry presented in Fig. 4.1. The x-z plane is the incident plane where z-axis is parallel to the surface normal. For SHG, the boundary condition determines that the exit angle β is equal to the incident angle.

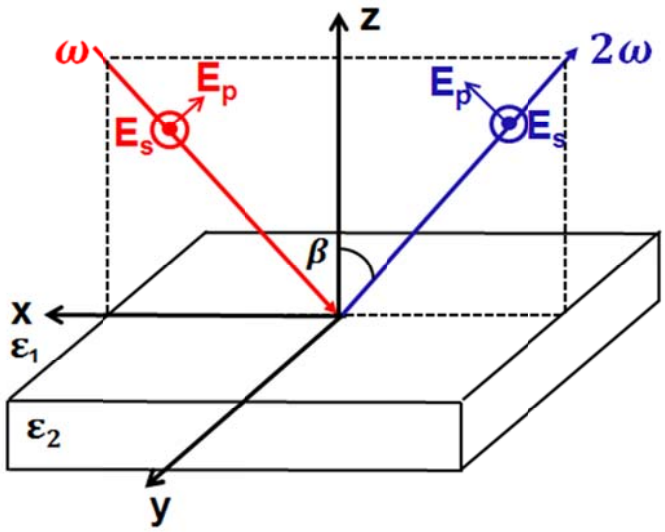

Figure 4.1 Geometry of second-harmonic generation.

The Fresnel coefficients for frequency ω at an interface of two media with dielectric constants $\varepsilon_1(\omega)$ and $\varepsilon_2(\omega)$ are [87]

$$L_{xx}(\omega) = \frac{2\varepsilon_1(\omega)k_{2z}(\omega)}{\varepsilon_2(\omega)k_{1z}(\omega) + \varepsilon_1(\omega)k_{2z}(\omega)}$$

$$L_{yy}(\omega) = \frac{2k_{1z}(\omega)}{k_{1z}(\omega) + k_{2z}(\omega)}$$

$$L_{zz}(\omega) = \frac{2\varepsilon_1(\omega)\varepsilon_2(\omega)k_{1z}(\omega)}{\varepsilon_2(\omega)k_{1z}(\omega) + \varepsilon_1(\omega_1)k_{2z}(\omega)} \frac{1}{\varepsilon'(\omega)} \tag{4.4}$$

where $\varepsilon'(\omega)$ is the effective dielectric constant of the interfacial layer [86]. For bulk contribution, it equals the bulk dielectric constant $\varepsilon_2(\omega)$, and for surface contribution, the microscopic local-field correction needs to be considered leading to $\varepsilon'(\omega) = \frac{\varepsilon_2(\omega)(\varepsilon_2(\omega)+5)}{4\varepsilon_2(\omega)+2}$.

The input and output beams can be chosen to be either perpendicular or parallel to the plane of incidence being S-and P-polarized, respectively. Thus, independent elements of $\vec{\vec{\chi}}^{(2)}_{eff}$ can be probed selectively by different polarization combinations. For SHG, the four beam polarization combinations can be generally written as,

$$\begin{aligned}
\chi^{(2)}_{SS} &= L_{yy}(2\omega)L^2_{yy}(\omega)\cdot\chi^{(2)}_{yyy} \\
\chi^{(2)}_{SP} &= -\cos\beta L_{xx}(2\omega)L^2_{yy}(\omega)\cdot\chi^{(2)}_{xyy} + \sin\beta L_{zz}(2\omega)L^2_{yy}(\omega)\cdot\chi^{(2)}_{zyy} \\
\chi^{(2)}_{PS} &= \cos^2\beta L_{yy}(2\omega)L^2_{xx}(\omega)\cdot\chi^{(2)}_{yxx} \\
&\quad + \cos\beta\sin\beta L_{yy}(2\omega)L_{xx}(\omega)L_{zz}(\omega)\cdot\chi^{(2)}_{yxz} \\
&\quad + \cos\beta\sin\beta L_{yy}(2\omega)L_{zz}(\omega)L_{xx}(\omega)\cdot\chi^{(2)}_{yxz} \\
&\quad + \sin^2\beta L_{yy}(2\omega)L^2_{zz}(\omega)\cdot\chi^{(2)}_{yzz} \\
\chi^{(2)}_{PP} &= -\cos^3\beta L_{xx}(2\omega)L^2_{xx}(\omega)\cdot\chi^{(2)}_{xxx} \\
&\quad - \cos^2\beta\sin\beta L_{xx}(2\omega)L_{xx}(\omega)L_{zz}(\omega)\cdot\chi^{(2)}_{xxz} \\
&\quad - \cos^2\beta\sin\beta L_{xx}(2\omega)L_{zz}(\omega)L_{xx}(\omega)\cdot\chi^{(2)}_{xzx} \\
&\quad + \cos\beta\sin^2\beta L_{xx}(2\omega)L^2_{zz}(\omega)\cdot\chi^{(2)}_{xzz} \\
&\quad + \cos^2\beta\sin\beta L_{zz}(2\omega)L^2_{xx}(\omega)\cdot\chi^{(2)}_{zxx} \\
&\quad + \cos\beta\sin^2\beta L_{zz}(2\omega)L_{xx}(\omega)L_{zz}(\omega)\cdot\chi^{(2)}_{zxz} \\
&\quad + \cos\beta\sin^2\beta L_{zz}(2\omega)L_{zz}(\omega)L_{xx}(\omega)\cdot\chi^{(2)}_{zzx} \\
&\quad + \sin^3\beta L_{zz}(2\omega)L^2_{zz}(\omega)\cdot\chi^{(2)}_{zzz}
\end{aligned} \tag{4.5}$$

The notation, for example, $\chi_{SP}^{(2)}$ refers that the input $\vec{E}(\omega)$ is S-polarized, and the output $\vec{E}(2\omega)$ is P-polarized. Also, the expression $\chi_{ijk}^{(2)}$ is specific to a certain coordinate system. It can be transformed from one coordinate system XYZ to another xyz as

$$\chi_{ijk}^{(2)} = \sum_{lmn} \chi_{lmn}^{(2)} (\hat{i} \cdot \hat{l})(\hat{j} \cdot \hat{m})(\hat{k} \cdot \hat{n}) \tag{4.6}$$

where ijk and lmn refers to the new coordinates xyz and original coordinates XYZ, respectively. The above description allows us to predict the non-vanishing susceptibility components in our measurements on the fishnet sample and silver film which is used for normalization.

4.3 Experimental setup

The laser system used for the experiment is well described in [88, 89]. The laser beams are provided by a OPG/OPA setup pumped by a mode-locked Nd:Yag laser (Continuum PY61C-20). Briefly, the oscillator stage of the Nd:Yag laser provides 25ps pulseas at 1.064um with 20Hz repetition rate. The output from the oscillator is focused to a pinhole to improve the mode quality by spatial filtering. After that the pulse is amplified to ~30mJ/pulse by a Nd:Yag amplifier. 75% of the energy is picked up to generate 355nm output by third harmonic generation. It is achieved by first generating second-harmonics by a type-I LBO (lithium triborate) crystal. Then the second harmonic is combined with the fundamental 1064nm beam in a type-II LBO crystal to generate the third harmonic output of ~7mJ/pulse. The third harmonic output at 355nm is split by a 50:50 beam splitter and directs the beam into two OPG/OPA setups [89]. For a OPG/OPA system, there are two BBO crystals. The pump beam at 355nm passes these two crystals where their optical axes are positioned oppositely so there is no overall beam displacement. The signal and idler beams generated by the optical parametric process are sent to a grating where the first-order diffracted beam is reflected back. The fundamental 355nm beam is separated by a dichroic mirror. It is retro-reflected to be combined with the seed again at the two BBO crystals. The amplified seed is then separated again with a dichroic mirror giving a total output ~450uJ/pulse at the idler wavelength 1.5um. The OPG/OPA output is tunable from 0.41um to 2.6um using both signal and idler beams. The schematic of the OPG/OPA setup is depicted in Fig. 4.2.

Figure 4.2 OPG/OPA setup

For the experiment, the idler beam is selected and focused on the sample with a spot size of ~500um^2. The layout of the SHG setup is presented in Fig. 4.3. The beam is incident at 45^o and the generated SHG pulses are measured in reflection direction. The signals are detected Hamamatsu R955 photomultiplier tube and gate integrator electronics after spectral filtering and polarization selection. The signals were normalized to that of replacing the fishnet sample with a silver film. The structure (Fig. 4.4) has been prepared by the same process described in Sec. 3.2.

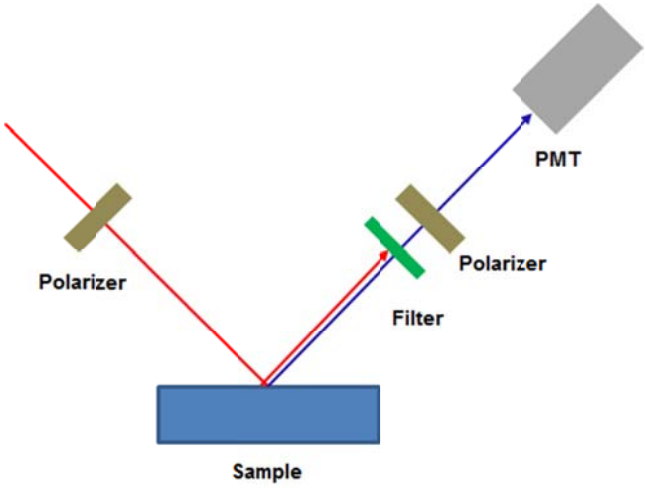

Figure 4.3 Experimental geometry for second-harmonic generation measurements.

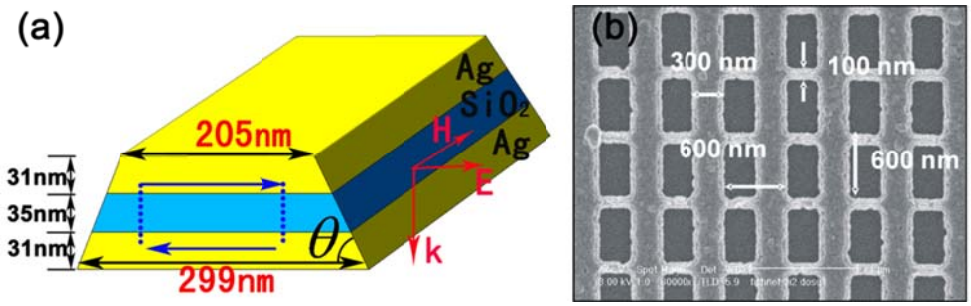

Figure 4.4 (a) Schematic of the thick wire of fishnet (b) SEM image

4.4 Results and analysis

4.4.1 Linear spectra of experiment and theoretical calculation

To understand the nonlinear optical response of a system, the linear optical properties should be known first. Therefore, we first carry out measurements to obtain transmission, reflection, and absorption spectra. The input beam with linear polarization along the thin stripes

normally impinging on the sample ($\vec{E} \parallel \vec{x}$ and $\vec{H} \parallel \hat{y}$, see Fig. 4.4(a)). The results are depicted in Fig. 4.5 by the red open circles, from which a magnetic resonance can be identified at ~1.375μm where the absorbance is maximum. Then a theoretical calculation is employed using a FDTD simulation [90]. The dielectric constants of silicon and silicon dioxide were taken as $3.4777 + i0.004$ and 1.65, respectively [91]. A Drude model was taken to describe the optical dielectric constant of silver $\varepsilon_r(\omega) = \varepsilon_\infty - \omega_{pl}^2 / \omega(\omega - i\omega_{col})$ with $\omega_{pl} = 1.37 \times 10^{16} s^{-1}$ and $\varepsilon_\infty = 4$. For thin silver films used in experiment, we expect electrons to experience additional scattering due to surface roughness and structural imperfections. Therefore, we set the damping parameter ω_{col} as an adjustable parameter to be determined by comparing with the experimental absorption spectrum. We found that the most appropriate value of ω_{col} was $9 \times 10^{13} s^{-1}$, which is roughly 6.6 times larger than the corresponding bulk value [51]. We note that similar adjustment was adopted in a recent theoretical study [38]. The FDTD calculated spectra with such a choice of ω_{col} are shown in Fig. 4.4 as blue lines, which are in excellent agreement with the experimental result. FDTD simulations identified the resonance at ~1.375μm to be a fundamental magnetic resonance and that at ~1.02μm a high-order magnetic resonance, since at both wavelengths strongly enhanced magnetic fields are induced inside the sandwich structure while the electric responses in the two Ag layers nearly cancel each other.

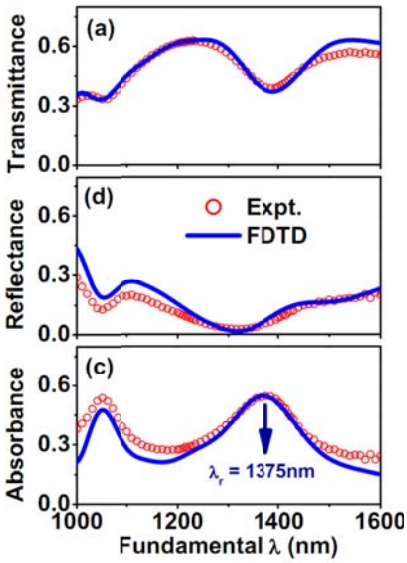

Figure 4.5 Linear transmission, reflection and absorption spectra of the double-fishnet metamaterial, obtained by experiments (red circles) and FDTD simulations (blue lines).

4.4.2 Computational methodology to calculate SHG spectra

The FDTD simulations provide the local electric field distribution of the input in the fishnet structure. This information is used to compute the nonlinear responses of the system. For example, Fig. 4.6 shows the distribution of local electric field on the x-z symmetry plane in the structure at 1.38μm with incident radiation of $\vec{E} \parallel \vec{x}$. The local field is strongly enhanced on

the inclined planes in regions close to the boundary between the top Ag layer and the middle SiO_2 layer.

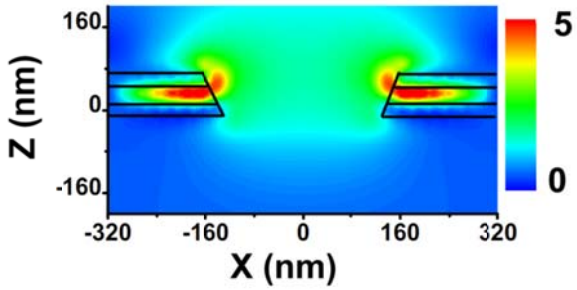

Figure 4.6 Normalized electric field distribution on the middle symmetrical x-z plane at 1.38μm.

The local field distribution is incorporated with a field integration technique to calculate the SHG signal. Here, the computational methodology is described briefly. For metal, the second-order nonlinear response is described by two independent, non-vanishing surface nonlinear susceptibilities $\chi^{(2)}_{S,\perp} \equiv \chi^{(2)}_{S,\zeta\zeta\zeta}$ and $\chi^{(2)}_{S,\parallel} \equiv \chi^{(2)}_{S,\xi\xi\zeta} = \chi^{(2)}_{S,\xi\zeta\xi} = \chi^{(2)}_{S,\eta\eta\zeta} = \chi^{(2)}_{S,\eta\zeta\eta}$, where ζ is along the surface normal. It is well known that $\chi^{(2)}_{S,\perp} \equiv \chi^{(2)}_{S,\zeta\zeta\zeta}$ dominates the response [92]. Therefore, in the calculation only this component is considered for flat Ag surfaces and local Ag surfaces of the metamaterial structure. Then the effective electric-dipole moment for SH radiation, $\vec{p}^{(2)}(2\omega)$, that is induced in a unit cell by an incoming field, $\vec{E}(\omega)$ can be expressed as [85, 93]

$$\vec{p}^{(2)} = \int \vec{L}(\vec{r},2\omega) : \vec{\chi}^{(2)}_S : [\vec{E}_{loc}(\vec{r},\omega)]^2 d\vec{r} \tag{4.7}$$

where the integration is over the entire silver surfaces within a unit cell.
$\vec{E}_{loc}(\vec{r},\omega) = \vec{\vec{L}}(\vec{r},\omega)\cdot\vec{E}(\omega)$ is the local electric field, and $\vec{\vec{L}}(\vec{r},\omega_i)$ is the local field correction factor at ω_i. They are obtained from the FDTD calculation. For a rough calculation, the integration in Eq. (4.7) is carried over the surface areas of a unit cell that are directly *exposed* to the incoming light.

We normalize the reflected SH signal from the fishnet against the reflected SH signal with P-in/P-out polarizations from a flat Ag surface. Thus, the signal can be expressed as

$$\frac{S_{\sigma'\sigma}}{S_{ref}} = \frac{\left|\hat{e}_\sigma \cdot \vec{p}^{(2)}(\sigma,\sigma')\right|^2}{\left|\hat{e}_p \cdot [\vec{p}^{(2)}(p,p)]_{ref}\right|^2}. \tag{4.8}$$

Here, $S_{\sigma'\sigma}$ denotes the signal generated with the σ'-in/σ-out polarization combination from the fishnet. $\hat{e}_\sigma$ (σ = S,P) is the unit vector for polarization σ. $\vec{p}^{(2)}(\sigma,\sigma')$ and $[\vec{p}^{(2)}(p,p)]_{ref}$

refer to the effective SH dipole moments per unit cell area on the sample and the flat Ag film, respectively, induced by inputs of the same intensity. For $[\vec{p}^{(2)}(p,p)]_{ref}$, Eq. (4.7) reduces to

$$[\vec{p}^{(2)}(p,p)]_{ref} = A\vec{\vec{L}}(\vec{r},2\omega):\vec{\vec{\chi}}_S^{(2)}:[\vec{\vec{L}}(\vec{r},\omega)\cdot\vec{E}_p(\omega)]^2 \tag{4.9}$$

where A is the area of the unit cell of the fishnet, and the local-field factor $\vec{\vec{L}}(\vec{r},\omega)$ is simply the transmission Fresnel coefficient for the air/metal interface.

4.4.3 SHG spectra of experiment and theoretical calculation

In the experiment, the reflected SHG spectra with various input/output polarization combinations are measured around the magnetic resonance. The sample is oriented so that the incident plane is either the y-z or the x-z plane (x and y being along and perpendicular to the thin stripes, respectively). The input beam angle on the sample is at $\alpha = 45^\circ$. The results are depicted in Fig. 4.7. The spectra are normalized against the SH signal of P-in/P-out polarization combination from a flat Ag film.

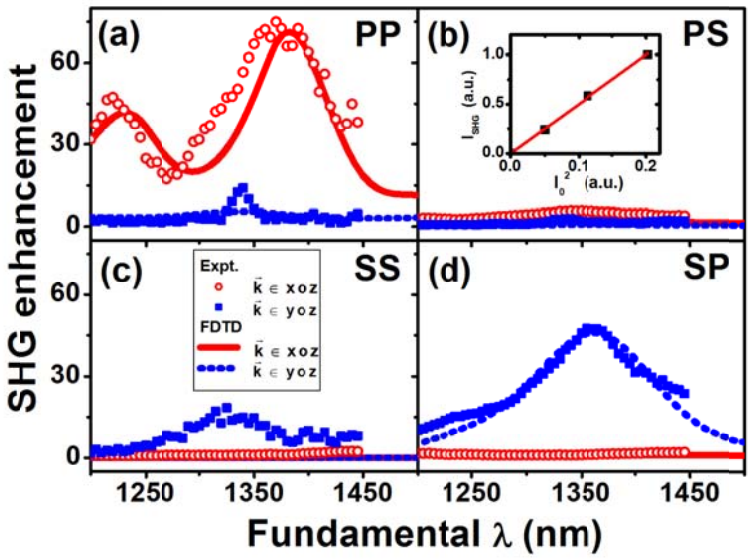

Figure 4.7 FDTD calculated (lines) and measured (symbols) SHG spectra of the fishnet structure for different polarization combinations: (a) P in, P out; (b) P in, S out; (c) S in, S out; (d) S in, P out. The incident angle is kept at $\alpha = 45^\circ$ and the incident planes are specified in the legend for different cases. Inset shows the measured quadratic dependence of the SHG signal on the incident pump power.

The calculated SHG spectra are compared with the experimentally measured spectra in Fig. 4.7. We find reasonable quantitative agreement between calculated and measured spectra. Several characteristic features of the SHG spectra from the fishnet are noticed. First, a resonant peak always appears around the magnetic resonance at $\sim 1.375\mu m$ as long as the input beam has a magnetic field component along $\hat{y}$, although the precise position of the resonance peak shifts slightly in different spectra compared to the normal incidence case (Fig. 4.5). Second, both theory and experiment show that the SHG enhancement for the P-in/P-out polarizations at the magnetic resonance is ~80 times in comparison with that on a flat silver surface. This is remarkable considering that the fishnet structure has nearly half of the surface plane empty. Third, the P-polarized SH output is much stronger than the S-polarized one, irrespective of the input polarization. Fourth, both theory and experiment display two resonant peeks in the P-in/P-out spectra; the peak at $\sim 1.22\mu m$ was *not* observed in the normal incidence spectra (Fig. 4.5) and the S-in/P-out SHG spectrum (Fig. 4.7(d)). Finally, the non-resonant SH signal with P-in/P-out polarizations is strong as we would expect, knowing that a strong PP-SHG is also observed on a flat silver film. The non-zero SHG signals in SS and PS cases observed experimentally are caused by imperfections of the real sample. Detailed discussions of the features are done in the following in the following section.

4.5 Discussions

The resonant enhancement of SHG from the fishnet around $1.375\mu m$ arises from resonant enhancement of the local field. For our fishnet structure, the magnetic resonance can be excited only when the input excitation has a magnetic field component along $\hat{y}$, and is observable in SHG with a P-polarized input propagating in the x-z plane or an S-polarized input propagating in the y-z plane. To explicitly illustrate the local field enhancement effect, Fig. 4.7(a) and (b) depicts the FDTD-calculated local field at the upper Ag/SiO_2 edge on the inclined side plane for S-polarized input in the y-z plane and P-polarized input in the x-z plane, respectively. In both cases, the fundamental resonance at $\sim 1.375\mu m$ is obvious. Interestingly, an additional weak resonance at $\sim 1.22\mu m$ is found in the P-input case (Fig. 4.8(b)), which does not exist in the S-input spectra (Fig. 4.8(a)) and the normal-incidence spectrum (Fig. 4.5(c)). FDTD simulations identified this resonance as an electric-dipole one with currents flowing on the side walls, and it can only be excited by an input wave with an E_z component (e.g., off-normal P-wave input). This resonance is also responsible for the peak at $\sim 1.22\mu m$ in the PP-SHG spectra (Fig. 4.6(a)), observed both experimentally and numerically.

The frequencies of resonances excited by S- and P-polarized inputs are slightly different (Fig. 4.8), and similarly for resonances observed in the SHG spectra with S- and P- inputs as shown in Fig. 4.7(a) and (d). This is due to different resonance dispersions in the two cases because of different couplings between adjacent magnetic resonators in the fishnet. Both our experiment and FDTD simulation revealed that the resonance dispersion of the S-input case is stronger than that of the P-input case, and thus, the former has a more red-shifted resonant frequency. The FDTD simulations have taken such effects into account rigorously.

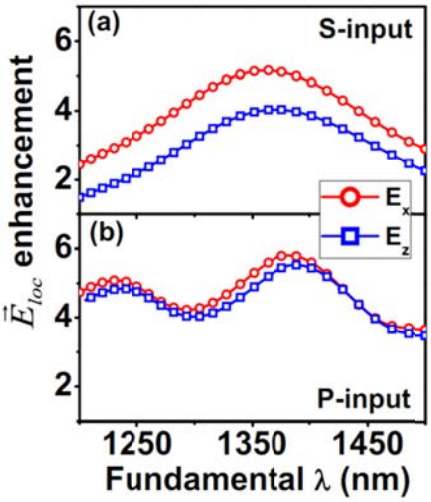

Figure 4.8 Normalized local fields at the Ag/SiO_2 edge in the inclined side plane as functions of the fundamental wavelength, calculated by FDTD simulations assuming (a) S-wave incident in the y-z plane and (b) P-wave incident in the x-z plane.

Relative strengths of SHG with different polarization combinations can be understood from symmetry argument. Eq. (4.7) can be re-written as

$$\vec{p}^{(2)}(2\omega) = \vec{\vec{X}}^{(2)} : \vec{E}(\omega)\vec{E}(\omega), \tag{4.10}$$

where $\vec{\vec{X}}^{(2)} = \int \vec{L}(\vec{r},2\omega) : \vec{\vec{\chi}}_S^{(2)} : \left[\vec{L}(\vec{r},\omega)\right]^2 d\vec{r}$ should reflect the symmetry of the unit cell. The fishnet structure has mirror planes at x=0 and y=0, then the nonvanishing elements of $\vec{\vec{X}}^{(2)}$ are $X_{zzz}^{(2)}$, $X_{zxx}^{(2)}$, $X_{zyy}^{(2)}$, $X_{xzx}^{(2)} = X_{xxz}^{(2)}$, and $X_{yzy}^{(2)} = X_{yyz}^{(2)}$. None of these elements contributes to SHG with P(-in)S(-out) and SS polarization combinations. Therefore, PS-SHG and SS-SHG are forbidden in such a fishnet structure. The experimentally observed signals shown in Fig. 4.7 appeared only because the real fishnet structure did not have the perfect mirror symmetry. On the other hand, SP- and PP-SHG are allowed. As mentioned above, the magnetic resonance is expected in SP-SHG with beams in the y-z plane and in PP-SHG with beams in the x-z plane. The corresponding contributing $\vec{\vec{X}}^{(2)}$ elements to SP-SHG and PP-SHG are $X_{zxx}^{(2)}$ and ($X_{zzz}^{(2)}$, $X_{zxx}^{(2)}$, $X_{xzx}^{(2)} = X_{xxz}^{(2)}$), respectively. We note here that in contrast to the flat metal surface, SP-SHG from the fishnet (with beams in the y-z plane) is non-vanishing even if we treat the metal as a free electron gas. This is mainly because SP-SHG can be generated from the inclined side planes of the fishnet structure. In our fishnet structure, SHG originates from the silver part of the surfaces. For SP-SHG, the P-polarized SH output comes solely from $p_z^{(2)}$ induced in each unit cell by the S-polarized input. Contribution from the top flat surface of the Ag stripes to $p_z^{(2)}$ is negligible if the local field component perpendicular to the surface is negligible. On the other hand, contribution from the Ag side planes is significant and is given by

$$p_z^{(2)} \sim \int \left\{ \begin{array}{l} \chi_{\perp}^{(2)} (E_{z,loc} \cos\theta + E_{x,loc} \sin\theta)^2 \cos\theta \\ -2\chi_{\parallel}^{(2)} (E_{x,loc} \cos\theta - E_{z,loc} \sin\theta)(E_{z,loc} \cos\theta + E_{x,loc} \sin\theta) \sin\theta \end{array} \right\} dS \qquad (4.11)$$

where θ is the inclination angle of the side planes (see Fig. 4.4), and the integration is over the Ag-covered area of the inclined side planes. Fig. 4.9 shows how $E_{x,loc}$ and $E_{z,loc}$ vary on the side wall and the top Ag surface for $\theta = 71^\circ$ (experimental sample) and $\theta = 90^\circ$ (ideal case with vertical side walls). It is seen that around the upper Ag/ SiO_2 edge on the side walls, the local field enhancement is near maximum. In addition, different symmetry properties possessed by $E_{x,loc}$ and $E_{z,loc}$ within a unit cell are actually responsible for the global symmetry of $\ddot{\mathrm{X}}^{(2)}$ elements which we argued before. At $\theta = 90^\circ$, both $E_{x,loc}$ and $E_{z,loc}$ are present even though the S-polarized input has *only* a field component along $\hat{x}$.

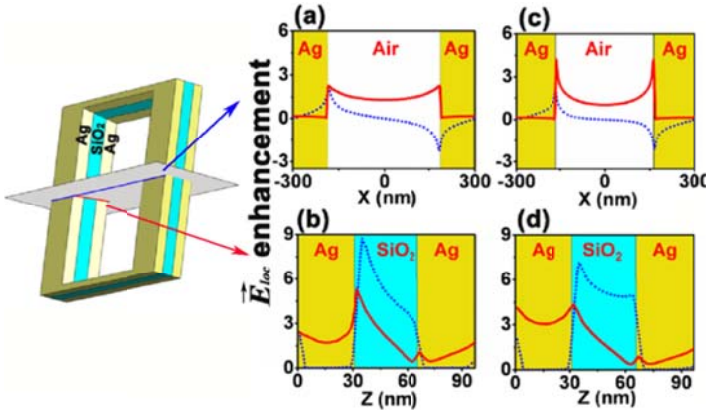

Figure 4.9 Distributions of normalized local fields (solid line: $E_{x,loc}$; dashed line: $E_{z,loc}$) along the symmetry lines on the top and the side wall Ag surface, calculated by FDTD simulations for the fishnet structures with (a)+(b) $\theta = 71^\circ$, and (c)+(d) $\theta = 90^\circ$.

Fig. 4.10 describes SHG from a fishnet with $\theta = 90^\circ$ obtained from FDTD simulations. It is seen, as expected, that SS- and PS-SHG do vanish, consistent with the symmetry argument presented above. Both PP- and PS-SHG are allowed, but PP-SHG is appreciably stronger than SP-SHG. It is interesting to compare the $\theta = 90^\circ$ case (Fig. 4.10) with the experimental sample case with $\theta = 71^\circ$ (Fig. 4.7). Because of the much stronger local-field enhancement, PP-SHG and SP-SHG for $\theta = 71^\circ$ are much stronger than those for $\theta = 90^\circ$.

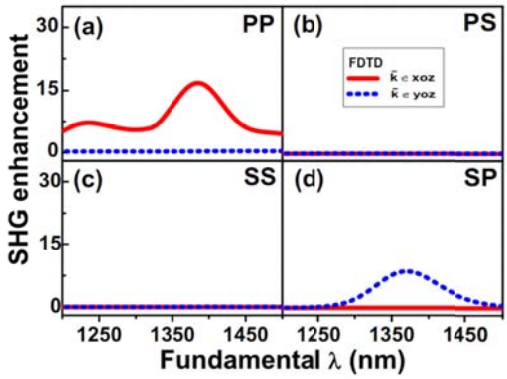

Figure 4.10 Simulated SHG spectra of the fishnet with vertical side walls: (a) P in P out, (b) P in S out, (c) S in S out, and (d) S in P out. Incident angle is kept as $\alpha = 45^{\circ}$ and the incident planes are specified in the legend for symbols and lines, respectively.

Finally, we note that the linewidth of the measured SHG peak (Fig. 4.7) is narrower than the linear absorption peak (Fig. 4.5). It was shown in [85] that the measured third harmonic generation (THG) peak is further narrowed compared with the SHG one. This is in striking contrast with resonance behaviors of molecular materials, where the linear, SHG, and THG spectra often have similar line shapes [86]. The difference arises because in metamaterials, the resonance enhancement is through the local field resonance. The *n*th harmonic in a metamaterial is generated by the *n*th-order induced polarization

$$\vec{p}^{(n)} = \int \vec{L}(\vec{r}, n\omega) : \vec{\chi}_{eff}^{(n)}(\vec{r}) : [\vec{E}_{loc}(\vec{r}, \omega)]^n d\vec{r} \qquad (4.12)$$

which can be approximated by $p^{(n)}(n\omega) \propto \left|\vec{L}(\vec{r}, \omega)\right|^n$ if "hot spots" exist. This explains the resonant linewidth narrowing of the higher harmonics.

4.6 Conclusions

In summary, using SHG spectroscopy and comparing it with theoretical calculations, we have provided a complete analysis of second harmonic responses from a fishnet metamaterial. It is shown that the resonant enhancement of SHG from a metamaterial is achieved through the resonant enhancement of the local field. In our case, we observed an enhancement of ~80 times larger signal compared to that of a bare silver film. Also, the excellent agreement between experiment and theory validates the computational approach of FDTD simulations with a field integration technique to calculate the nonlinear response. It may be utilized to further understand details of many interesting phenomena observed experimentally, and allow researchers to design optimal metamaterial structures for nonlinear wave-mixing applications.

Chapter 5

Pump-probe spectroscopy study of fishnet metamaterial

5.1 Motivation

Actively controlling the optical properties of metamaterials have garnered much interest because of the potential implications [94, 95]. By changing the effective refractive index upon request, one can envision tuning the functioning frequency range of negative refractive index materials or invisibility cloaking devices. In addition, tuning the properties of metamaterials can also be useful in improving the performance of conventional applications such as modulation and switching [96]. Recent studies have mostly focused on switching by utilizing low-frequency metamaterials through applying a bias voltage [97]. However, in these studies the spectral behavior changes of effective optical constants are not studied and therefore provide only limited understanding. Also, since the switching is achieved by applying bias voltage, the speed is limited by the time constant of the equivalent circuit. Therefore it is impossible to probe the intrinsic limit of switching speed.

In this chapter, we report our study carrying out femtosecond pump-probe spectroscopy to probe the modulation dynamics of a fishnet metamaterial [64]. We have designed a new kind of fishnet metamaterial with a mid-semiconductor layer and utilized optical pumping to excite free carriers in the nanostructure. Very short pulses are required to probe the intrinsic limit of the dynamics of the materials. Therefore we use femtosecond pulses to probe the dynamical change of metamaterials. The results help elucidate how the effective optical constants change upon external perturbations.

5.2 Experiment

5.2.1 Fishnet design

We design a new type of fishnet structure that includes an amorphous silicon (*a*-Si) layer. The purpose of including a semiconductor layer is to allow excitation of free carriers upon optical pumping. Our sample is composed of Ag(25nm)/*a*-Si(80nm)/Ag(25nm) sandwiched layers on a silica substrate. Fig. 5.1 presents a scanning electron microscope (SEM) image (Fig. 5.1(a)) and the schematics of the three dimensional structure (Fig. 5.1(b)). The samples were designed using the finite-difference-time-domain (FDTD) method [90] to have a magnetic response in the near-infrared. Adjusting the width and thicknesses of the grids along with selecting material of proper dielectric constants allows fine tuning of the resonant frequency to the desired value [98]. The samples were prepared by nanoimprint lithography [69]. During the evaporation process, *a*-Si was evaporated between the top and bottom silver layers.

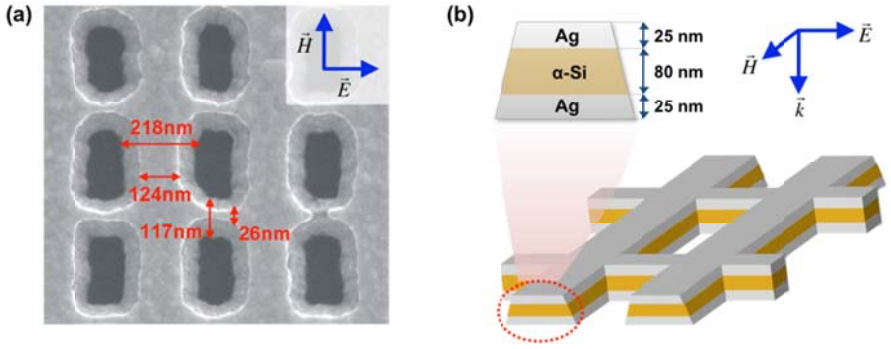

Figure 5.1 Fishnet structure (a) SEM image of a sample. Its grid-like structure is composed of orthogonal thin and thick wires. (b) Schematic of the fishnet showing the Ag/*a*-Si/Ag sandwiched layers.

5.2.2 Experimental setup

Fig. 5.2 depicts the experimental arrangement.. To explain briefly, it implements a Michelson-type interferometer to measure the magnitude and phase of the transmission and reflection coefficients. A 20-MHz super-continuum fiber laser providing a broadband wavelength between 500-1650nm was used to probe the sample without pump. For the pump-probe studies, a femtosecond laser system was utilized. A 1-kHz Ti:Sapphire regenerative amplifier was use to pump an optical parametric amplifier (OPA) system. The amplifier provides 100-fs pulses at 800 nm and is used to pump the fishnet metamaterial. The OPA provides tunable near-infrared pulses (1.05-3.3μm) and probes the metamaterial. Details of the regenerative amplifier and OPA system are described in [99].

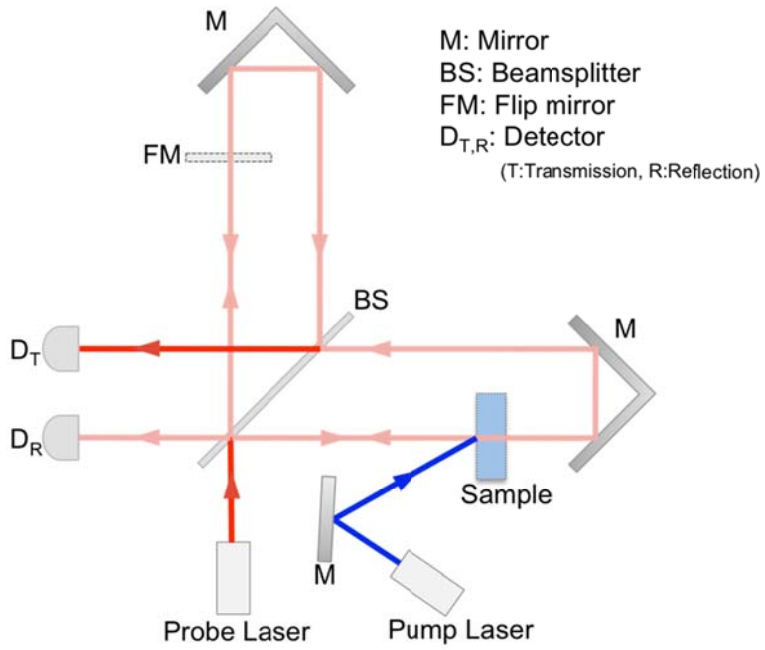

Figure 5.2 Experimental setup to measure the complex transmission ($\hat{t}$) and reflection ($\hat{r}$) coefficients.

5.3 Results and analyses

5.3.1 Pump-induced changes of magnitude, phase, and effective optical constants

First, the magnitude and phases of the complex $\hat{t}$ and $\hat{r}$ coefficients are measured without the optical pump. Blue solid lines in Fig. 5.3(a,b,d,e) display the measured $T=|\hat{t}|^2$, $R=|\hat{r}|^2$, ϕ_t, and ϕ_r, respectively. Then following the procedure in Sec. 3.2, we deduce the complex effective refractive index ($\hat{n}$) and impedance ($\hat{z}$). Next, the optical pump is introduced and the changes in the amplitude and phase of $\hat{t}$ and $\hat{r}$ are measured using a lock-in technique. The pump-induced changes of $\Delta T/T$, $\Delta R/R$, $\Delta\phi_t$ and $\Delta\phi_r$ at pump fluence of 300μJ/cm^2 are plotted in Fig. 5.3(c,f). By adding the pump-induced changes to metamaterial linear responses, transmission and reflection parameters with the pump are obtained and shown as the red dashed lines in Fig. 5.3(a,b,d,e).

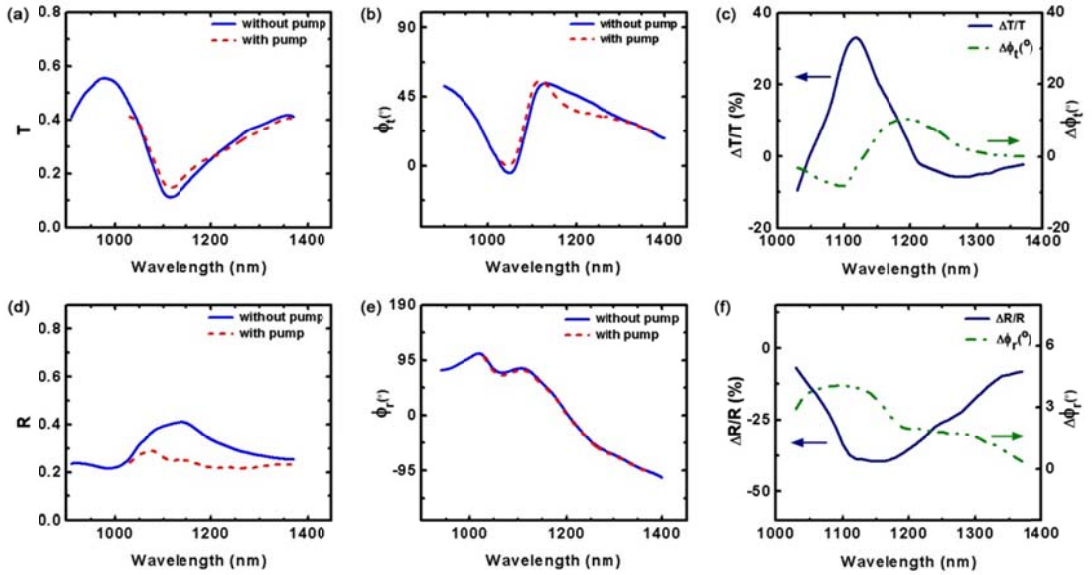

Figure 5.3 Experimentally measured spectra of T, R, ϕ_t and ϕ_r with and without pump. (a) T. (b) ϕ_t. (c) ΔT/T and $\Delta\phi_t$. (d) R. (e) ϕ_r. (f) ΔR/R and $\Delta\phi_r$.

Fig. 5.4 plots the deduced effective $\hat{n}$, $\hat{\varepsilon}$, $\hat{\mu}$ and their modulations from the measurements. The dip in T and peak in R clearly shows a characteristic resonant spectral feature. The distinct resonant features of $\hat{\mu}$ confirm a strong magnetic resonance at 1.15μm where the resonant wavelength defined by the peak of Im($\hat{\mu}$). The pump-induced spectral changes of all quantities around the resonance are also clearly observed. The Re($\hat{\varepsilon}$) also exhibits spectral features at the magnetic resonance, indicating that the resonance is not purely magnetic, a result arising from the tapered layer structure of the fishnet (Fig. 5.2(b)) that causes mixing of the usual symmetric and asymmetric resonant modes [56].

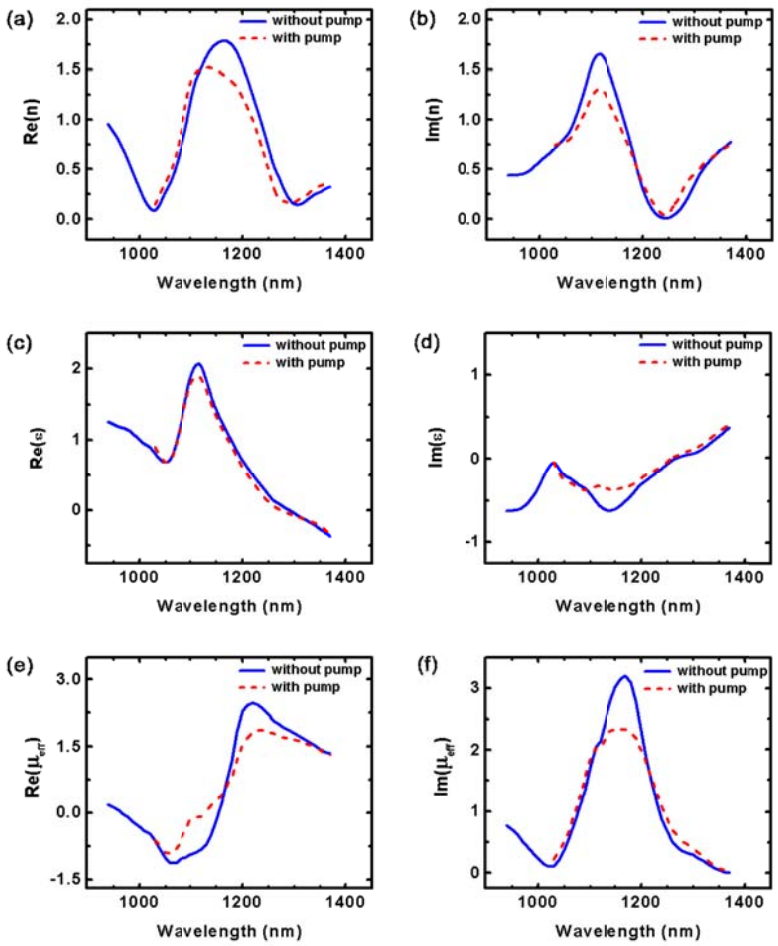

Figure 5.4 Experimentally deduced $\hat{n}$, $\hat{\varepsilon}$ and $\hat{\mu}$ from $\hat{t}$ and $\hat{r}$ with and without pump. (a) Re($\hat{n}$). (b) Im($\hat{n}$). (c) Re($\hat{\varepsilon}$). (d) Im($\hat{\varepsilon}$). (e) Re($\hat{\mu}$). (f) Im($\hat{\mu}$). The blue solid and red dash curves are deduced from those of (a,b,d,e) of Fig. 5.3.

The spectra of $\hat{\mu}$ in Fig. 5.4(e) and 5.4(f) shows that the pump-induced changes come in mainly through broadening of the magnetic resonance. This results from the induced refractive index changes, Δn^{f} and Δk^{f}, of *a*-Si in fishnet. These can be estimated from the refractive index change, Δn^{b} and Δk^{b}, of the bare *a*-Si film, which are deduced from the measured changes of transmittivity (T^{b}) and reflectivity (R^{b}) of the film using the relations [100],

$$\Delta \mathrm{T}^{\mathrm{b}} = \left(\frac{\partial \mathrm{T}^{\mathrm{b}}}{\partial n^{\mathrm{b}}}\right)\Delta n^{\mathrm{b}} + \left(\frac{\partial \mathrm{T}^{\mathrm{b}}}{\partial k^{\mathrm{b}}}\right)\Delta k^{\mathrm{b}} \text{ and } \Delta \mathrm{R}^{\mathrm{b}} = \left(\frac{\partial \mathrm{R}^{\mathrm{b}}}{\partial n^{\mathrm{b}}}\right)\Delta n^{\mathrm{b}} + \left(\frac{\partial \mathrm{R}^{\mathrm{b}}}{\partial k^{\mathrm{b}}}\right)\Delta k^{\mathrm{b}}. \qquad (5.1)$$

The experimentally obtained values are Δn^{b}=-0.01 and Δk^{b}=0.05. Δn^{f} and Δk^{f}, being similar to these values, are mainly responsible for the shift and broadening of the magnetic resonance,

respectively. In our case, the shift of resonance is not appreciable, and only the effect of Δk^{f} is significant. In general, however, one could use both Δn^{f} and Δk^{f} to shift and broaden the resonance to achieve strong modulation. Large Δn^{f} alone could be obtained in dielectric materials such as liquid crystals and polyelectrolytes.

Interestingly, we also note that Fig. 5.3(c) show correlations between pump-induced changes of different quantities. The maximum ΔT occurs around minimum $\Delta\phi_t$ and vice versa, at 1.12μm and 1.2μm, respectively. This can be readily understood from the Kramers-Kronig relations. Therefore, both amplitude and phase modulations are achievable and can be predicted from understanding of how the optical constants behave under external perturbation.

5.3.2 Modulation strength

The pump-induced change is most significant near the resonance as expected. The normalized induced changes are observed to be ΔT/T=31% and ΔR/R= -42% at the resonance wavelength 1.12μm for a pump fluence of 300μJ/cm^2 and zero pump-probe time delay. Fig. 5.5(a) also shows that the changes are linear with the pump fluence. The decrease in Im($\hat{n}$), which mainly follows from decrease of Im($\hat{\mu}$) at the magnetic resonance (Fig. 5.4(b) and 5.4(f)), leads to the different signs of ΔT and ΔR. Interestingly, the observed ΔT/T and ΔR/R on an *a*-Si film (same thickness (80nm) as that in the fishnet structure) were both less than 1% with the same pump fluence. Thus, the pump-induced changes of ΔT/T and ΔR/R in the metamaterial structure are 50 times larger than that of bare *a*-Si thin film. The significantly larger signal comes from enhancement through the plasmon resonance: a small change in the refractive index of the dielectric layer in the metamaterial can induce a dramatic change in the resonant characteristics, and hence the optical properties near resonance. Therefore, metamaterials can be a very effective optical modulator.

5.3.2 Modulation speed

The relaxations of ΔT/T and ΔR/R after pumping were measured for both the fishnet and *a*-Si film. Then the relaxation of the pump-induced absorption change (ΔA) is deduced. The pump-induced absorptions in both cases are very similar as shown in Fig. 5.5(b). The induced changes as function of probe-pump time delay have a fast decay component of ~750fs followed by a long tail extending over hundred picoseconds. The similar decay dynamics of *a*-Si and the fishnet incorporating it indicate that the fishnet modulation dynamics is dominated by free carrier excitation in *a*-Si. The contribution from excited carriers in the metal layers is negligible because the maximum excited carrier density in the silver layer estimated from the pump fluence is ~10^{18}cm^{-3}. This is orders of magnitude smaller than the intrinsic free carrier density ~10^{23}cm^{-3}, and therefore its effect on the optical properties of the fishnet is insignificant. Therefore, dielectric materials with larger absorption coefficient and shorter carrier lifetime should be chosen in order to improve the strength and speed of the pump-induced modulation. For example, low-temperature grown GaAs is known to have carrier lifetimes of ~200fs [101]

and so is ion-implanted InP [102]. Both have strong direct interband absorption that can lead to large modulation depth with lower pump fluence.

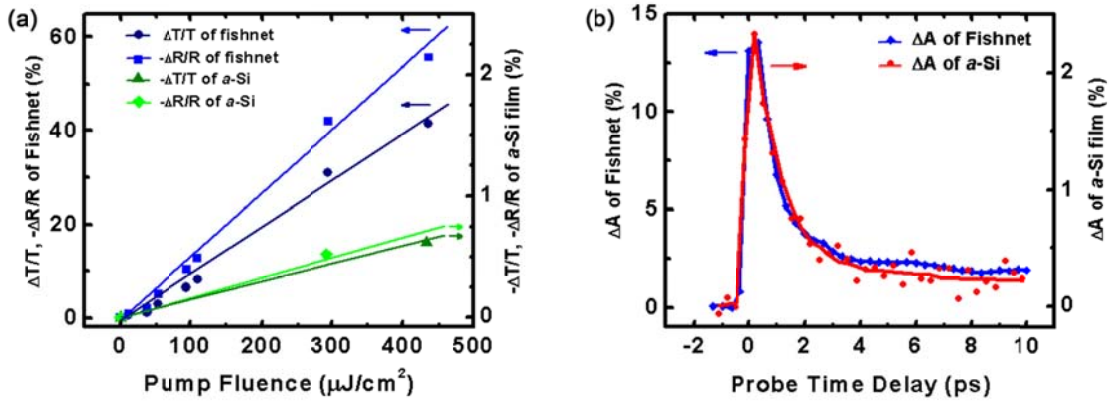

Figure 5.6 Pump-induced responses of the fishnet and *a*-Si film. (a) Normalized changes of transmission and reflection versus pump fluence. (b) Pump-induced absorptions versus probe-pump time delay.

5.4 Conclusions

We have carried out femtosecond pump-probe spectroscopy with an interferometer to measure the pump-induced spectral changes of transmission, reflection and their phases over the magnetic plasmon resonance of a metamaterial. By doing so, we are able to study the spectral and dynamic behavior of optical modulation in the fishnet structure. The observed pump-induced changes had a fast relaxation time of ~750fs, and the magnitude of change was dramatically enhanced compared to that in natural materials. The spectral changes indicated that the effect is mainly due to the pump-induced broadening of the resonance. The modulation was governed by the properties of the dielectric layer in the fishnet. Its relaxation time corresponded to the excited carrier lifetime of the dielectric medium. The results indicate that stronger and faster modulation could be achieved by proper choice of the dielectric medium in the metamaterial structure. Our study suggests that further improvement of the modulation characteristics is possible with better choice of the dielectric medium.

Bibliography

[1] L. Esaki, and R. Tsu, Ibm J Res Dev **14** (1970).
[2] J. D. Joannopoulos, P. R. Villeneuve, and S. H. Fan, Nature **387** (1997).
[3] M. Husnik *et al.*, Nat Photonics **2** (2008).
[4] J. Henzie *et al.*, Annu Rev Phys Chem **60** (2009).
[5] S. R. J. Brueck, P Ieee **93** (2005).
[6] W. Cai, and V. Shalaev, *Optical Metamaterials* (Springer, 2010).
[7] L. D. Landau, E. M. Lifshitz, and J. B. Sykes, *Electrodynamics of continuous media* (Pergamon Press, 1960).
[8] R. E. Camley, and D. L. Mills, Phys Rev B **26** (1982).
[9] L. Remer *et al.*, Phys Rev Lett **56** (1986).
[10] J. B. Pendry *et al.*, Ieee T Microw Theory **47** (1999).
[11] T. J. Yen *et al.*, Science **303** (2004).
[12] M. W. Klein *et al.*, Opt Lett **31** (2006).
[13] J. B. Pendry *et al.*, Phys Rev Lett **76** (1996).
[14] D. R. Smith *et al.*, Phys Rev Lett **84** (2000).
[15] V. G. Veselago, Sov. Phys. Usp. **10** (1968).
[16] S. Xi *et al.*, Phys Rev Lett **103** (2009).
[17] S. Zhang *et al.*, Phys Rev Lett **95** (2005).
[18] J. Yao *et al.*, Science **321** (2008).
[19] V. M. Shalaev, Nat Photonics **1** (2007).
[20] N. Fang *et al.*, Science **308** (2005).
[21] J. B. Pendry, Phys Rev Lett **85** (2000).
[22] Z. Jacob, L. V. Alekseyev, and E. Narimanov, Opt Express **14** (2006).
[23] Z. W. Liu *et al.*, Nano Lett **7** (2007).
[24] Z. W. Liu *et al.*, Science **315** (2007).
[25] T. Taubner *et al.*, Science **313** (2006).
[26] U. Leonhardt, Science **312** (2006).
[27] U. Leonhardt, and T. Tyc, Science **323** (2009).
[28] J. S. Li, and J. B. Pendry, Phys Rev Lett **101** (2008).
[29] J. B. Pendry, D. Schurig, and D. R. Smith, Science **312** (2006).
[30] D. Schurig *et al.*, Science **314** (2006).
[31] V. M. Shalaev, Science **322** (2008).
[32] J. Valentine *et al.*, Nat Mater **8** (2009).
[33] R. A. Shelby, D. R. Smith, and S. Schultz, Science **292** (2001).
[34] D. R. Smith, J. B. Pendry, and M. C. K. Wiltshire, Science **305** (2004).
[35] G. V. Eleftheriades, A. K. Iyer, and P. C. Kremer, Ieee T Microw Theory **50** (2002).
[36] C. G. Parazzoli *et al.*, Phys Rev Lett **90** (2003).
[37] M. Bayindir *et al.*, Appl Phys Lett **81** (2002).
[38] S. Linden *et al.*, Science **306** (2004).
[39] G. Dolling *et al.*, Science **312** (2006).
[40] G. Dolling *et al.*, Opt Lett **30** (2005).
[41] G. Dolling *et al.*, Opt Lett **32** (2007).

[42] A. N. Grigorenko *et al.*, Nature **438** (2005).
[43] V. A. Podolskiy, A. K. Sarychev, and V. M. Shalaev, J Nonlinear Opt Phys **11** (2002).
[44] V. M. Shalaev *et al.*, Opt Lett **30** (2005).
[45] C. M. Soukoulis, S. Linden, and M. Wegener, Science **315** (2007).
[46] A. Alu, and N. Engheta, J Opt Soc Am B **23** (2006).
[47] R. A. Depine, and A. Lakhtakia, Microw Opt Techn Let **41** (2004).
[48] S. Zhang *et al.*, Phys Rev Lett **94** (2005).
[49] B. T. Draine, and P. J. Flatau, *User Guide for the Discrete Dipole Approximation Code DDSCAT 6.1* 2004).
[50] M. A. Yurkin, and A. Hoekstra, *Amsterdam DDA, version 0.77* 2007).
[51] P. B. Johnson, and R. W. Christy, Phys Rev B **6** (1972).
[52] J. D. Jackson, *Classical Electrodynamics* (Wiley, New York, 1979).
[53] V. M. Agranovich *et al.*, Phys Rev B **69** (2004).
[54] R. E. Raab, and O. L. D. Lange, *Multipole Theory in Electromagnetism* (Oxford Science, New York, 2005).
[55] V. M. Agranovich, and Y. N. Garstein, Phys. Usp. **49** (2006).
[56] D. J. Cho *et al.*, Phys Rev B **78** (2008).
[57] K. B. Alici, and E. Ozbay, Opt Lett **34** (2009).
[58] D. R. Smith, D. Schurig, and J. J. Mock, Phys Rev E **74** (2006).
[59] T. Driscoll *et al.*, Phys Rev B **75** (2007).
[60] S. N. Burokur, T. Lepetit, and A. de Lustrac, Appl Phys Lett **95** (2009).
[61] C. Menzel *et al.*, Appl Phys Lett **95** (2009).
[62] C. Menzel *et al.*, Phys Rev B **81** (2010).
[63] C. Menzel *et al.*, Phys Rev B **77** (2008).
[64] S. Zhang *et al.*, Opt Express **13** (2005).
[65] K. M. Dani *et al.*, Nano Lett **9** (2009).
[66] K. M. Dani, Opt Express **19** (2011).
[67] G. Dolling *et al.*, Appl Phys Lett **89** (2006).
[68] S. Y. Chou, P. R. Krauss, and P. J. Renstrom, J Vac Sci Technol B **14** (1996).
[69] W. Wu *et al.*, Appl Phys a-Mater **87** (2007).
[70] H. F. Ghaemi *et al.*, Phys Rev B **58** (1998).
[71] S. G. Rodrigo, F. J. Garcia-Vidal, and L. Martin-Moreno, Phys Rev B **77** (2008).
[72] U. Schroter, and D. Heitmann, Phys Rev B **58** (1998).
[73] T. Thio *et al.*, Nanotechnology **13** (2002).
[74] Y. R. Shen, and F. DeMartini, in *Surface Polaritons*, edited by V. M. Agranovich, and D. L. Mills (North-Holland Publishing Co., 1982), p. 629.
[75] E. N. Economou, Physical Review **182** (1969).
[76] A. Bondeson, *Computational Electromagnetics* (Springer, 2000).
[77] E. D. Palik, *Handbook optical constants of solids* 1991).
[78] E. Popov, L. Mashev, and D. Maystre, Optica Acta **33** (1986).
[79] S. Gasiorowicz, *Quantum Physics* (Wiley, 1996), 2nd edn.
[80] H. R. Philipp, and E. A. Taft, Physical Review **113** (1959).
[81] Z. Ku, and S. R. J. Brueck, Opt Express **15** (2007).
[82] E. Pshenay-Severin *et al.*, J Opt Soc Am B **27** (2010).
[83] M. W. Klein *et al.*, Science **313** (2006).
[84] M. W. Klein *et al.*, Opt Express **15** (2007).

[85] E. Kim *et al.*, Phys Rev B **78** (2008).
[86] Y. R. Shen, P Natl Acad Sci USA **93** (1996).
[87] X. Zhuang *et al.*, Phys Rev B **59** (1999).
[88] W. Liu, (University of California at Berkeley, 2008).
[89] D. Kim, (University of California at Berkeley, 1998).
[90] A. Taflove, and S. Hagness, *Comupational Electrodynamics: The Finite-Difference Time-Domain Method* (Artech House, 2005).
[91] E. D. Palik, *Handbook of optical constants of solids* (Academic, San Diego, 1998).
[92] J. Rudnick, and E. A. Stern, Phys Rev B **4** (1971).
[93] Y. R. Shen, *Principles of Nonlinear Optics* (Wiley, New York, 1984).
[94] H. T. Chen *et al.*, Nat Photonics **3** (2009).
[95] E. Kim *et al.*, Appl Phys Lett **91** (2007).
[96] K. F. MacDonald *et al.*, Nat Photonics **3** (2009).
[97] H. T. Chen *et al.*, Nature **444** (2006).
[98] W. Wu *et al.*, Appl Phys a-Mater **95** (2009).
[99] J. Mcguire, 2004).
[100] M. Kubinyi, A. Grofcsik, and W. J. Jones, J Mol Struct **408** (1997).
[101] E. S. Harmon *et al.*, Appl Phys Lett **63** (1993).
[102] C. Carmody *et al.*, J Appl Phys **94** (2003).